FIBER OPTIC BASED FORCE SENSOR DESIGN FOR PROSTATE BIOPSY PROCEDURE UNDER MRI

by

Nurettin Okan Ülgen

B.Sc., Electrical & Electronics Engineering, Boğaziçi University, 2016

Submitted to the Institute of Biomedical Engineering
in partial fulfillment of the requirements
for the degree of
Master of Science
in
Biomedical Engineering

Boğaziçi University
2018

FIBER OPTIC BASED FORCE SENSOR DESIGN FOR PROSTATE BIOPSY PROCEDURE UNDER MRI

APPROVED BY:

Assoc. Prof. Dr. Özgür Kocatürk (Thesis Advisor)	....
Prof. Dr. Yekta Ülgen	....
Prof. Dr. Murat Gülsoy	....

DATE OF APPROVAL: 19 June 2018

ACKNOWLEDGMENTS

Above all, the greatest thanks belong to my lovely family, my father Erden Ülgen, my mother Lale Betül Ülgen, and my brother Ziya Onur Ülgen, who are always supportive and loving. I am happy to make one of my dreams come true with their support, and I dedicate this thesis to them.

I am very grateful to my thesis advisor Assoc. Prof. Dr. Özgür Kocatürk for believing in the potential of me and motivating me through academic work that is outstanding and promising. His inspiring leading in this project made me love scientific and academic work more and more. I will always take his foreseeing and hardworking as an example throughout my life.

It is an honor for me to have Prof. Dr. Yekta Ülgen and Prof. Dr. Murat Gülsoy as committee members for my thesis dissertation. Their instructive contribution for the project is very substantial. Also, many thanks to Prof. Dr. Murat Gülsoy for his allowance to access Biophotonics Laboratory to use optical tools which were essential for the project, and I appreciate his lectures which provided me with the basis to comprehensively manage my studies in this project. I owe endless thanks to my fellow teammate, Doğangün Uzun, for his devotion to our work and communion in every aspect of the project. I would also like to thank to Ahmet Turan Talaş, Özgür Kaya, and Korel Yıldırım for their sincere helpfulness and courtesy. I have overcome many difficulties of the project thanks to their assistance and guidance with their expertness.

Cheers to JokerPub and all of my dear friends who made this period of time enjoyable. I am also deeply thankful to my beloved partner, Hülya Ceren Topgül, who made all of this meaningful and worthwhile.

This project is supported by Tübitak Project No:115E271 research grant.

ACADEMIC ETHICS AND INTEGRITY STATEMENT

I, Nurettin Okan Ülgen, hereby certify that I am aware of the Academic Ethics and Integrity Policy issued by the Council of Higher Education (YÖK) and I fully acknowledge all the consequences due to its violation by plagiarism or any other way.

Name : Signature:

Date:

ABSTRACT

FIBER OPTIC BASED FORCE SENSOR DESIGN FOR PROSTATE BIOPSY PROCEDURE UNDER MRI

Fabry-Pérot Interferometry (FPI) fiber optic sensors with low error ratio and high sensitivity can provide reliable feedback to optimize needle insertion for MRI-guided prostate biopsy. FPI based force sensing has also potential for diagnosis of prostate cancer (PCa) directly by providing data regarding mechanical characteristics of the tissue.In this thesis, design and fabrication of a fiber optic sensor based on FPI for force measurement at the tip of an prostate biopsy needle (18-gauge) is presented. The sensor is built upon an air cavity between two cleaved optical fibers with a diameter of 125 μm which are embedded and fixed into a borosilicate glass capillary with an inner diameter of 200 μm. Fixation of optical fibers within the glass capillary are achieved by applying medical grade UV adhesives through two micro-holes formed with CO_2 laser processing on the glass capillary. The initial distance between the fiber endings is adjusted by using manipulators controlled by piezoelectric actuators and strain gauge readers with a resolution of 10 nm. A laser diode which has a wavelength of 635 nm is used as a light source for the operation of the sensor. The intensity from the laser diode is kept constant during operation with current feedback mechanisms and temperature controllers. Model predictive control approaches are adapted and implemented for the temperature control of the light source. A circuitry for the operational control of the system and signal processing is implemented. The sensor is calibrated and optimized with a commercial pressure sensor and a force testing machine. Dynamic range of the sensor is set to the linear operation region to avoid signal ambiguity while being able to provide a force measurement range of 0-13 N with a resolution of 0.1 N based on needle insertion experiments conducted.

Keywords: Optical Fiber Sensors, Fabry-Pérot Interferometry (FPI), Force Sensor, Needle Insertion, MR Compatibility, MRI Guided Prostate Biopsy.

ÖZET

MRG ALTINDA PROSTAT BİYOPSİ PROSEDÜRÜ İÇİN FİBER OPTİK TABANLI KUVVET SENSÖRÜ TASARIMI

Düşük hata oranı ve yüksek hassasiyete sahip Fabry-Pérot İnterferometri (FPI) fiber optik sensörler MRG altında prostat biyopsisi için iğne girişini optimize etmek için güvenilir geri bildirim sağlayabilir. Bununla birlikte FPI tabanlı kuvvet algılamasının, dokunun mekanik özellikleri ile ilgili veriler sağlayarak prostat kanserinin (PCa) doğrudan teşhisinde kullanılma potansiyeli vardır. Bu tezde, 18-ölçü bir prostat biyopsi iğnesi ucunda kuvvet ölçümü için FPI bazlı bir fiber optik sensörünün tasarımı ve üretimi sunulmaktadır. Sensör, 200 μm iç çapa sahip bir borosilikat cam tüp içine yerleştirilmiş ve sabitlenmiş 125 μm çapındaki iki kesik optik fiberin arasında oluşturulan bir hava boşluğu ile kurulmuştur. Optik fiberlerin cam tüpün içine sabitlenmesi, cam tüp üzerinde CO_2 lazer işlemiyle oluşturulan iki mikro-delikten tıbbi dereceli UV yapıştırıcıların uygulanmasıyla sağlanmıştır. Fiber optiklerin uçları arasındaki uzaklık, piezoelektrik aktüatörler tarafından kontrol edilen manipülatörler ve 10 nm'lik bir çözünürlük ile gerinim ölçer okuyucuları kullanılarak ayarlanmıştır. Sensörün çalışması için ışık kaynağı olarak 635 nm dalga boyuna sahip bir lazer diyot kullanılmaktadır. Lazer diyotunun şiddeti, akım geri besleme mekanizmaları ve sıcaklık kontrolörleri ile sabit tutulmuştur. Model öngörülü kontrol yaklaşımları, ışık kaynağının sıcaklık kontrolü için uyarlanıp ve uygulanmıştır. Sistemin operasyonel kontrolü için bir devre kurularak ve sinyal işleme yapılmaktadır. Sensör, bir ticari basınç sensörü ve bir kuvvet test makinesi ile kalibre ve optimize edilmiştir. Sensörün dinamik aralığı, sinyal belirsizliğini önlemek için lineer çalışma bölgesine ayarlanmıştır ve gerçekleştirilen iğne yerleştirme deneylerinden elde edilen sonuçlara göre 0.1 N'lik bir çözünürlükle 0-13 N'luk bir kuvvet ölçüm aralığı sağlayabilmektedir.

Anahtar Sözcükler: Optik Fiber Sensörler, Fabry-Pérot İnterferometri (FPI), Kuvvet Sensöü, İğne Sokulması, MR Uyumluluğu, MRG Altında Prostat Biyopsisi.

TABLE OF CONTENTS

LIST OF FIGURES

LIST OF TABLES

LIST OF SYMBOLS

E	Young's modulus
R	Reflectance
T	Transmittance
n	Refractive index
L	Cavity length
F	Finesse
E	Electric field
A	Amplitude
I	Light intensity
K_p	Proportional term
K_d	Derivative term
K_i	Integral term
p	Pressure
r	Radius
L_{gauge}	Gauge length
P	Power
μ	Poisson's ratio
Φ	Phase of FPI
λ	Wavelength of incident light beam
Φ_o	Phase shift of FPI
Δ	Optical path difference
δ	Phase shift
ν	Visibility
θ_c	Critical angle
Δd_F	Change in effective cavity length
$f_1(\Delta F)$	Function axial forces
$f_2(\Delta T)$	Function temperature variations

LIST OF ABBREVIATIONS

FPI	Fabry-Perot Interferometry
PCa	Prostate Cancer
PSA	Prostate-Specific Antigen
DRE	Digital Rectal Examination
TRUS	Transrectal Ultrasound
MRI	Magnetic Resonance Imaging
MRE	Magnetic Resonance Elastography
EMI	Electromagnetic Interference
RFI	Radio Frequency Interference
NA	Numerical Aperture
RI	Refractive Index
MI	Michelson Interferometer
SI	Sagnac Interferometer
MZI	Mach-Zender Interferometer
OPD	Optical Path Difference
FSR	Free Spectral Range
SNR	Signal to Noise Ratio
MPC	Model Predictive Control
TEC	Thermoelectric Cooler

1. INTRODUCTION

In conventional prostate biopsies, the ability of the operator or the physician to sense the tissue is significantly reduced. One of the biggest problems that can be experienced in prostate biopsy is the deviation of the biopsy needle during operation and deviation from the desired target to be reached. The amount of bending of the biopsy needle can vary depending on the material and dimensions of the needle, the depth of intervention, and the force applied. In order for the biopsy needle to follow the most precise way during operation, it is important to sense force and indirectly the deformation of the needle with a force gauge sensor, as well as visualize the needle under the MRI, for the success of the operation.

With a biopsy needle design that receives feedback with fiber optic force sensors, success rates in operations can be significantly increased. Optically-based sensors stand out compared to conventional sensors because they cause no artifacts on MRI images and they are not affected by the electromagnetic fields contained within the MRI. Parameters such as force, pressure or position can be measured under MRI by using optical measurement sensors. In the literature, there are optical measurement sensors based on different principles which are considered in detail according to the priorities of prostate biopsy procedures. In the preliminary studies, it has been determined that the most suitable optical measurement method for the prostate biopsy procedure under MRI is the measurement based on the Fabry Perot Interferometry (FPI) principle.

Optical fiber based FPI sensors are intrinsically safe for clinical use thanks to being non-toxic and chemically inert. Their dielectric nature and small profile also allow their easy installation into miniaturized devices [1]. These advantages show that Fabry-Pérot fiber optic force sensors are suitable for the needle tip force measurements during MRI guided prostate biopsy operations.

2. PROSTATE CANCER

Prostate cancer (PCa) is currently the second most diagnosed cancer among men throughout the world [2]. The most recent statistics indicates that PCa remains a major cause of mortality among men even though deaths due to PCa is decreasing in most of the developed countries [3].

Etiology of prostate cancer is not well-understood yet and screening methods for PCa is still questionable. Evidences are also insufficient to correlate populations risks and lifestyle habits to diagnosis rates of PCa. In most of the cases, there occurs a comparatively slow progression of prostate cancer. Most of the tumors are trapped in the prostate and clinical appearance is rare throughout the lifetime of the patient. Tumors in prostate cancer are inert and death results from challenging matters before the clinical indications. The symptoms are clearly observable only until PCa is at a highly developed stage. Rectal examinations and increase in Prostate-Specific Antigen (PSA) levels indicates potentiality for PCa, and diagnosis requires biopsy.

For the survival of patients with prostate cancer, diagnosis should be done at early stages of the disease. Corresponding 5-year survival rates among patients with local tumors are approximately 100% [4]. However, patients having a distributed transition have a survival rate of about 28% for corresponding 5-year [5]. The number of incidence with organ-confined and regional diseases increases thanks to better diagnostic approaches for prostate cancer and there is a significant drop in the figures of progressive diseases [6].

Initial approaches for diagnosis include the clinical analyses with a digital rectal examination, and blood tests to quantify PSA. Suspicious results from these examinations requires use of advanced diagnostic approaches, which are transrectal ultrasound monitoring and biopsy procedures guided by different imaging modalities.

2.1 Conventional Methods for Diagnosis of Prostate Cancer

Detection and analysis of prostate cancer can be made in several ways at varying stages. It s also important to consider that patient examinations are not driven from symptoms of the disease for most of the cases.

2.1.1 Clinical Examinations

(a) Digital Rectal Examination (DRE)

Usual physical investigation of prostate organ aims to analyze the firmness of prostate and existence of nodules that can be localized or generalized. It is observed that about 30% of men above age 60 have some symptoms that can be associated to prostate cancer, which shows the importance of proper physical examination of prostate. 10% of the non-cutaneous abnormalities in men caused by prostate cancer for 10% of men aged above 60. Autopsy samples taken from men died after the age 80 have prostatic carcinoma nearly 50% of the time. Local extensions or other distinct metastases occur between 60% to 70% of the cases. Therefore, imperative and useful treatment is only possible when an early biopsy is done when there are any suspected abnormalities in prostate [7].

(b) Blood Examination

Prostate-Specific Antigen (PSA) is a widely applied clinical instrument used in diagnosis of prostate cancer. PSA blood tests are also used following stages of the treatment and monitoring after the treatment. PSA production increases in tissues with PCa, and borders of tissues between gland lumen and veins corrupts as a result of prostate carcinoma. Hence, more PSA is transferred to the serum and PSA levels in blood increases significantly in patients with PCa. It is shown by clinical studies that PSA raising can be 5-10 years before clinical diagnosis of the disease [8].

2.1.2 Transrectal Ultrasound (TRUS)

TRUS is the most preferable imaging modality compared to other available imaging modalities used for diagnosis of prostate cancer. The size of prostate also can be estimated by using transrectal ultrasound, and it can guide needle interventions through prostate. However, its use is limited to confirm prostate cancer after PSA level test and DRE instead of a primary tool to monitor prostate cancer. There occur technical problems in the use of TRUS due to technological limitations and observer differences in scanning. Therefore, there is lack of evidence on the accuracy and effectiveness of transrectal ultrasound approach to identify and diagnose prostate cancer [9].

2.1.3 Transrectal Ultrasound Guided Biopsy

After PSA level tests and DRE, needle biopsy is applied for more detailed information on the histology of prostate. The number of biopsy operation has a trend to increase significantly with the more common use of PSA level tests in urological practices throughout the world.

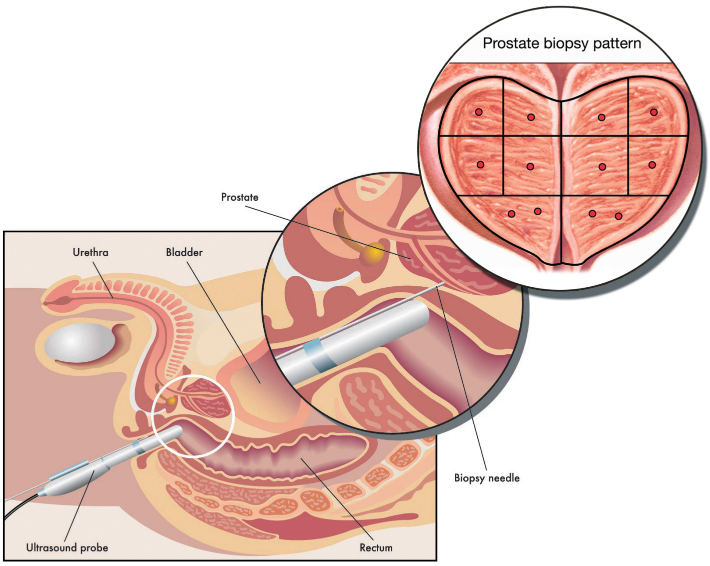

Figure 2.1 TRUS guided biopsy and biopsy pattern.

A spring-loaded biopsy gun manually triggered by the operators is used to insert an 18-gauge needle into prostate. TRUS is commonly used to target to suspected lesion and guide the needle. However, cells with prostate cancer can show different characteristics that can be difficult to differentiate with ultrasound technology. Therefore, a standard protocol of biopsy is followed most of the time during which 12 samples from different lesions of prostate are taken due to lack of precise targeting [10]. Locations of biopsy sample cores targeted during the procedure according to the common protocols are shown in Figure 2.1 [11].

2.1.4 MRI Guided Prostate Biopsy

The current gold-standard for prostate cancer diagnosis is biopsy during which samples are taken from targeted lesions of prostate. MRI-guidance has an increasing potential to meet the needs for targeting lesions during minimally invasive interventions of prostate biopsy [12].

MRI guided biopsy ensures that targeted suspicious regions of tissue is visualized during biopsy and placement of the needle is tracked toward the target. Hence, the accuracy of the procedure increases significantly and this results in higher rates of cancer detection [13]. Another advantage of MRI guided biopsy is that fewer number of sample cores from the regions that are suspicious for intermediate or high risk PCa is sufficient for higher rates of cancer detection [14]. Targeting guided by MRI is not prone to motion, segmentation, and registration errors which is the case for MRI/TRUS fusion targeting approaches [15]. It is also possible to use MR images in order to analyze and detect tumor lesions with the help of recent developments in MRI technologies. Another improvement for reliably ascertaining PCa is sensing tissue characteristics during the procedures [16]. Magnetic resonance elastography (MRE), which is based on modified phase-contrast MRI sequences and shear wave propagation, is a highly promising and innovative approach which is used for analysis of soft tissues [17]. However, use of MRE for detection of PCa is very limited since producing shear wave propagation with required amount of frequencies and amplitudes is not possible in most of the cases [18].

These limitations which lower spatial resolution of MRE needs to be addresses for clinical application of this non-invasive cancer detection approach.

A needle guide system such as shown in Figure 2.2 [19] is required to use for MRI guided biopsy procedures since limited space of MRI bore makes it difficult to reach patient, and orientation of the needle guide and the needle itself needs to be adjusted precisely and accurately throughout the procedure [20]. This biopsy platform, which is placed and fixed onto MRI scanner table, enables placement, angular alignment, and advancement of the biopsy needle. However, tactile sensing by the operator regarding advancement of biopsy needle through tissues is limited, which impose a need for real-time force sensing mechanisms for MRI guided prostate biopsy procedures.

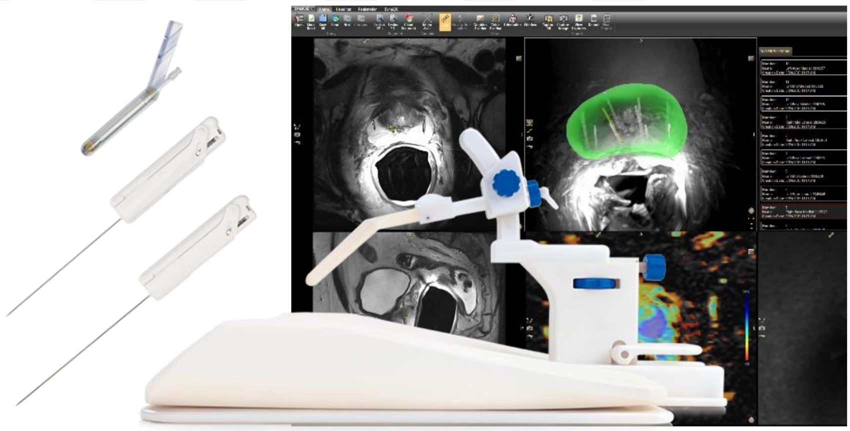

Figure 2.2 Needle guide mechanism and software for MRI guided prostate piopsy.

Steps published by RSNA as a protocol for MRI guided prostate biopsy procedure are listed below [21]:

1. Multiparametric MR images are acquired for diagnostic purposes.
2. Patient is administered an antibiotic and placed prone to MRI table.
3. Coils are put on the back of the patient.
4. Needle gun is integrated to the MR-compatible biopsy device.
5. Biopsy device is inserted through the rectum.
6. T2-weighted MR images are acquired for calibration.
7. Suspected lesions in prostate are redefined.

8. Orientation of biopsy needle is arranged via software.
9. Needle guide is set according required positioning.
10. Positioning is rechecked with T2-weighted images.
11. Optimal positioning is ensured with further adjustments.
12. Needle firing mechanism is integrated to the system.
13. Needle firing mechanism is triggered.
14. Position of the needle is observed with T2-weighted images.
15. Two or more samples are taken from suspected lesions.
16. Patient is assisted to arise from the table since there is a risk of fall.
17. Patient is observed for 30 minutes.

2.2 Fiber Optic Based Force Sensing for Prostate Biopsy

Conventional prostate biopsy procedure is performed under ultrasound imaging [22]. However, using ultrasound imaging for biopsy needle guidance might cause inaccurate needle biopsy of prostate tumors due to poor tissue contrast [23]. Magnetic Resonance Imaging (MRI) is more convenient for real time interventional prostate biopsy procedures compared to ultrasound thanks to its superior soft tissue contrast and high spatial resolution [24].

Several studies have shown that elasticity may provide valuable information for differentiation of malignant prostate cancer and benign or normal prostate tissue. It is known that collagen deposition of malignant prostate cancer cells increases significantly, which directly determines the elasticity of the tissues [25, 26, 27]. In excised prostate tissues, stiffness of malignant regions increases 2-3 fold compared to healthy tissues [28, 29, 30]. These finding reveal the importance of biomechanical sensing for detection of PCa. It can be stated that integration of a force sensing mechanism would be highly beneficial to improve cancer detection rates in prostate biopsy procedures under MRI.

During MRI-guided needle insertion procedures, force sensing has potential to provide meaningful feedback which can ensure practical safety and improve accuracy of insertion [31]. By measuring the needle insertion force using MRI compatible sensor, a critical feedback information about the anatomical location and any potential deflection of the biopsy needle will be determined in real time. This can improve the overall procedure success rate while decreasing the need for multiple biopsy operations.

Magnetic Resonance Imaging provides high contrast tissue imaging that enables better targeting capabilities for interventional procedures. Even though recent improvements in MRI resulting in higher quality images with reduced acquisition times, tactile force measurement is still an essential feedback especially for needle-based interventions. Optical force sensing is a method that can be confidently used for providing reliable feedback in order to ensure safety and accuracy of MRI-guided prostate biopsy [31]. An optical force feedback mechanism will help optimize needle insertion based on force and tissue deformation. It can also be useful for diagnosis of PCa directly by providing data to differentiate different types of tissues regarding mechanical characteristics.

Measurement of a physical parameter such as force, pressure or strain is challenging task (during MR imaging) due to electromagnetic interferences (EMI) and radio frequency interferences (RFI). However, optical force sensors are immune to EMI and RFI. Measurements based on optical sensors are also safe to use in medical applications since there is no electricity used for the sensing mechanisms. Use of light instead of electricity is another significant advantage of optical force sensors because there are not any inherent limitations such as potential crosstalk between cables, RF heating of cables and other devices. On the other hand, conventional force sensors that contains long conductors might cause serious harm to the patient due to RF heating. Also, optical force sensors are more favorable choice for MRI guided interventions due to low signal attenuation when precise measurements are needed and signals carrying useful information is needed to be processed remotely from the sensing side. Biocompatible and chemically inert materials can be used for the manufacturing of optical force sensors, which makes those convenient to use in medical applications. Optical force sensing is a perfectly suitable tool in MRI guided interventions with its unique features of which defining ones mentioned above.

Sensors based on optical fibers outperform compared to other conventional sensors for force, pressure, or strain sensing with the outstanding features summarized and listed as follows:

(a) Design
- Inert Materials (Glass, Polyimide etc.)
- Robust Packaging
- Small Size

(b) Environment
- Cryogenic to high temperature
- Chemical Resistance
- EMI Insensitive
- In situ Monitoring

(c) Signal Processing
- Low Signal Attenuation
- Temperature Compensable

(d) Other
- Biocompatibility & Sterilization
- Intrinsically Safe
- Light-weight
- Low-cost

3. OPTICAL FIBER SENSORS

3.1 Principles of Operation

The main principle behind optical fiber sensors can be explained with modulation of some parameters such as intensity, wavelength, phase and polarization of an optical fiber system which is measured as changes in the output signal received with the help of optical detectors. An external physical phenomenon that induce variations on optical properties of light being transmitted through optical fiber can be detected and measured based on this principle.

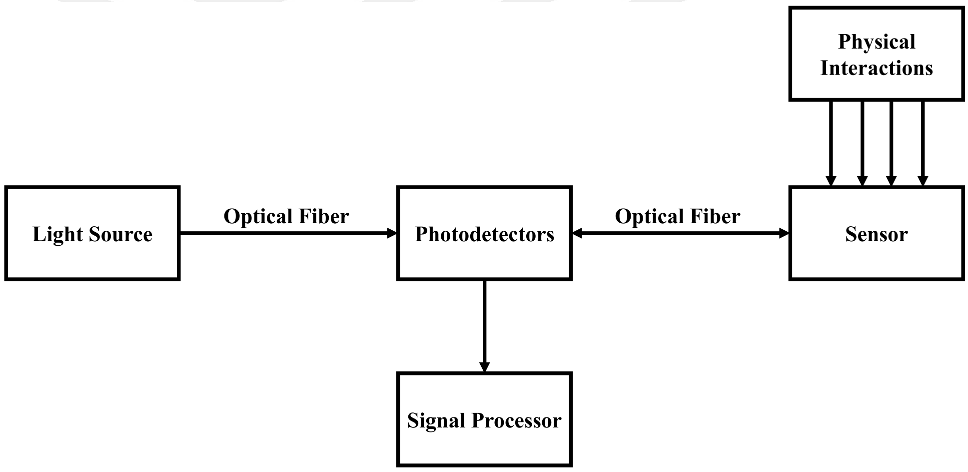

Figure 3.1 Working principle of optical fiber sensors.

3.2 Fundamental Elements

3.2.1 Optical Fibers

Optical fibers can be used as a transmission medium in which propagating light carrying an information from a mechanism independent from the fiber itself or as a sensing element which converts an outside effect to modulation of light. Use of optical fibers as sensing elements provides several advantages such as low attenuation, immunity to electromagnetic interference (EMI), low cost, and compact size which are important factors for interventional procedures under MRI.

Light inside the optical fiber internally reflects while it propagates forwards. The cladding of optical fiber which has a lower refractive index compared to the core of optical fiber enable this continuous internal reflection and propagation.

As seen in Figure 3.2, an incident light with initial angle smaller than $\theta_{\max}$ is able to propagate through fiber optic according to Snell's law.

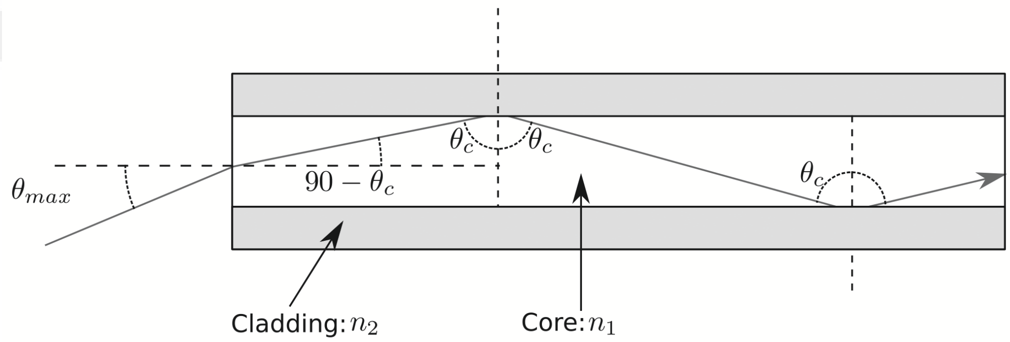

Figure 3.2 Propogation of light inside optical fiber.

The critical angle θ_c in Figure 3.2 can be defined as follows in 3.1 where n_{clad} stands for refractive index of the cladding of the fiber and n_{core} stands for refractive index of the core of the fiber.

$$\theta_c = \sin^{-1}(\frac{n_{clad}}{n_{core}}) \tag{3.1}$$

The numerical aperture (NA) of optical fiber, which is the measure of ability to accept light with large incident angles, can be derived from the Equation 3.1 as:

$$NA = n_{core}\sin(\pi/2 - \theta_c) = \sqrt{n_{core}^2 - n_{cladding}^2} \tag{3.2}$$

3.2.2 Light Sources

Light sources are used to establish optical fiber sensor system with production of required amount of light by spontaneous or stimulated emission processes. Most commonly used light sources for optical fiber sensing can be categorized as given in the Table 3.2.2:

Table 3.1
Common light sources for optical fiber sensors.

Wavelength (nm)	Material	Lifetime (h)	Cost	Availability
<500	Nd:YAG	≥10,000	Moderate-High	Moderate
600-700	InGaP/InGaAIP	≥10,000	Moderate	Limited
700-900	GaAlAs/GaAs	10,000-30,000	Low-Moderate	Very Good
900-1700	InGaAsP/InP	≥100,000	Moderate-High	Good

Semiconductor light sources are more preferable because of their miniature size, low cost, long life time with stable operation, and low power consumption.

When a semiconductor arranged such a way that light emitting region is limited and confined, required energy for stimulated emission is reached and a laser diode is created. Output of a laser diode is mostly based on spontaneous emission for low input currents while it is dominated by stimulated emission for higher currents as seen in Figure 3.3.

Laser diodes can be considered very susceptible to feedback, which is a key issue that determines the performance of an optical fiber sensor based on laser diode [32]. When light back reflects to laser cavity, effective light intensity in the cavity changes dramatically depending on the phase and coherence difference of back reflected light and the light in the cavity. Fiber pigtails are the first cause of significant back reflection, and hence single-mode fiber is preferred to couple the emitted light in order to guarantee high performance of the optical system. A circular symmetric output is desired for the coupling of light with the highest efficiency.

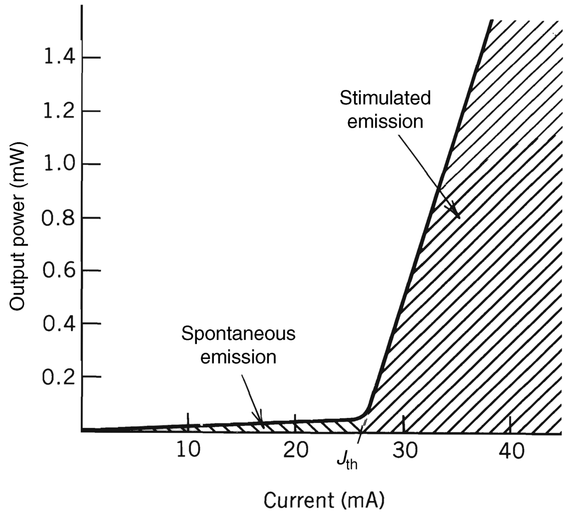

Figure 3.3 Output of a typical laser diode with respect to input current.

Variations in ambient temperature is another issue to be considered for high performance of laser diodes. Figure 3.4 illustrates the effect of temperature on laser output power. The current needed to reach emission threshold increases as the temperature increases, and the slope of output power-diode current curve decreases. Output power of a laser source operating with a current feedback control loop drops significantly with increasing temperature, which results in inconsistent and erroneous measurements. Temperature has also effects on some other main characteristics of a laser which result in shifts in bandwidth and wavelength of the beam emitted from the laser diode. Photovoltaic response of photodetectors, on the other hand, is highly dependent on wavelength. Hence, variations in wavelength cause incorrect interpretations from the sensing system.

3.2.3 Optical Detectors

Photodetectors are sensor used for detection of light with p-n junctions or p-i-n junctions where p stands for p-type material carrying positive charge, n stands for n-type material carrying negative charge, and i stands for intrinsic material creating depletion region where light is absorbed. Photodetectors can be categorized into four as p-n junction photodetectors, p-i-n junction photodetectors, avalanche photodetec-

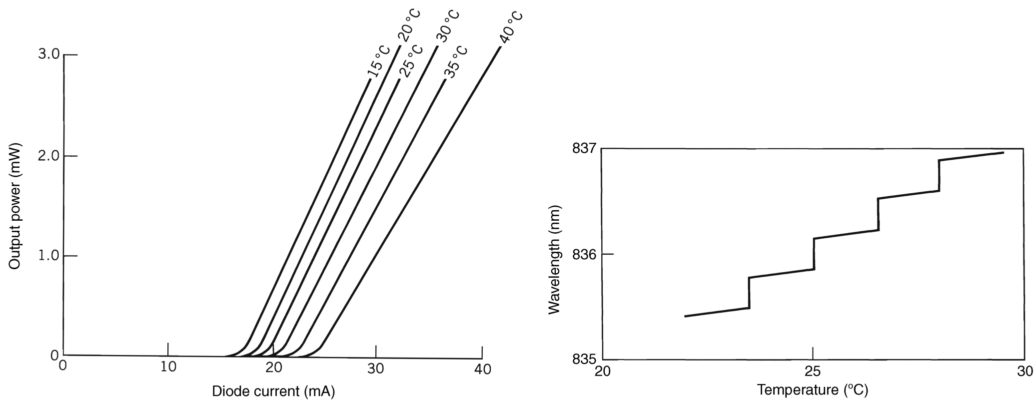

Figure 3.4 Effects of temperature change on laser operation.

tors, and Schottky photodetectors. Basic p-n junction photodetectors works based on electrons and holes created by absorption of photons within a p-n semiconductor junction. If this junction is configured specifically, charge buildups can be detected and measured in photovoltaic mode or photo-conductive mode depending on the type of the circuit. High resistivity material between p and n layers seen in Figure 3.5 increases the amount of incident photons absorbed in the depletion region, and hence a larger charge separation is achieved.

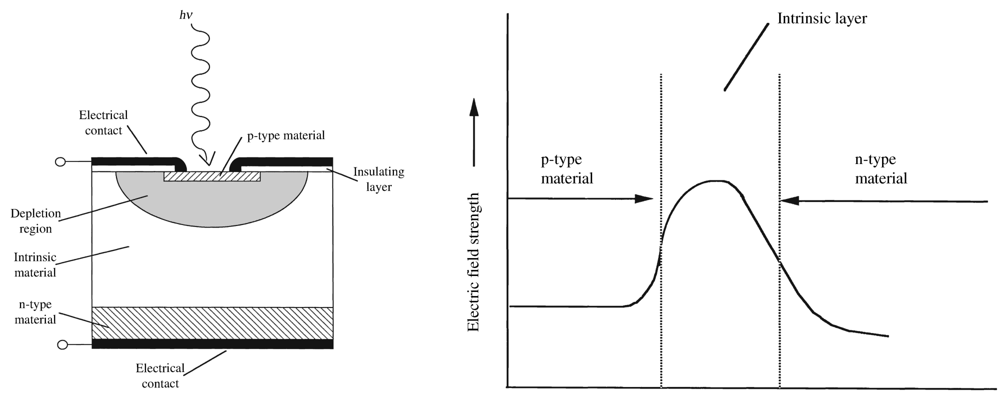

Figure 3.5 Working principles of silicon photodiodes.

When this p-i-n junction is reverse biased, an avalanche photodetector is constructed which works based on initiation avalanche breakdown with incoming light and internal gain due to formation of more carriers. A more advanced photodiode can be constructed with multiple layers namely absorption, multiplication, charge, and grading regions separated from each other. Photodetectors with a metal semiconductor junction which provides a very low forward voltage drop are named as Schottky photodetectors. For optical fiber sensing devices, three layered junctions of p-i-n are more suitable compared to other types of photodetectors structures.

Photovoltaic response with respect to wavelength of a typical silicon photodetector can be illustrated as given in Figure 3.6. Other measures of performance for

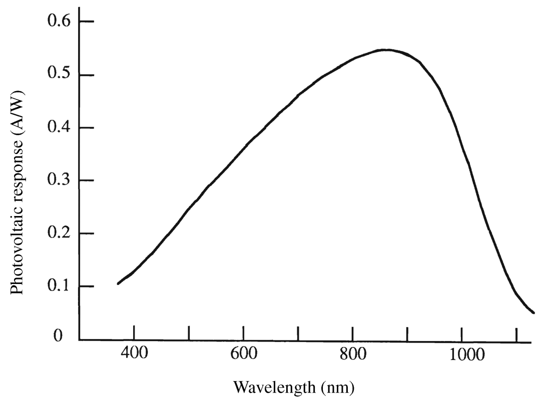

Figure 3.6 Response curve of a typical silicon photodiode.

photodetectors are spectral response, quantum efficiency, detectivity, noise equivalent light power, response time, dark current, and noise spectrum.

3.3 Classification of Optical Fiber Sensors

Optical fiber sensors are classified in different aspects as follows:

(a) Based on Working Principle
- Intensity-modulated sensors
- Phase-modulated sensors

(b) Based on Location
- Intrinsic
- Extrinsic

(c) Based on Measurement Parameters

- Physical sensors
- Chemical sensors
- Biosensors

Intensity modulated sensors gives an output which is proportional to the amount of impact to the sensing mechanism. Transmission, reflection, micro-bending, absorption, scattering, fluorescence, and polarization are main concepts associated with intensity based optical fiber sensors [33]. Such sensors require higher amount of light intensity for sufficient resolution since intensity of light is highly changeable based on the application [34]. Hence, multimode fibers with large diameter of core are more common for the configurations of intensity-modulated sensors. Phase modulated sensors, on the other hand, are usually consist of single mode fibers that are used as reference and sensing mediums. Phase of the light reflected back from the surfaces of two fibers separated with a cavity is compared for measurements, which is a more reliable and stable approach for sensing compared to intensity based sensors.

An extensive categorization of interferometric optical fiber sensors can be made based on the working principles. Types of interferometric optical fiber sensors and various applications of them are summarized in Figure 3.7 [32].

The most common types of optical fiber sensors based on interferometry are Michelson Interferometer (MI), Fabry Perot interferometer (FPI), Sagnac Interferometer (SI), and Mach-Zender Interferometer (MZI). In MI configurations, the light beams are separated to two paths and reflected back from the end of these paths. The difference between paths is adjusted such that it does not exceed optical coherence length of the laser. MI based sensors are commonly used in a variety of applications of temperature measurements,, strain measurement, refractive index measurements, and liquid analyses [35, 36, 37, 38]. Sensors configured with MZI has some similar properties with MI sensors in terms of separation of the beams into two arms. In MZI, one of the arms is used as reference arm and the other one is used as sensing arm. Simultaneous measurements of parameters (strain, temperature,refractive index) are possible by using MZI sensors. MI and MZI sensors differ from each other in use of reflection modes in

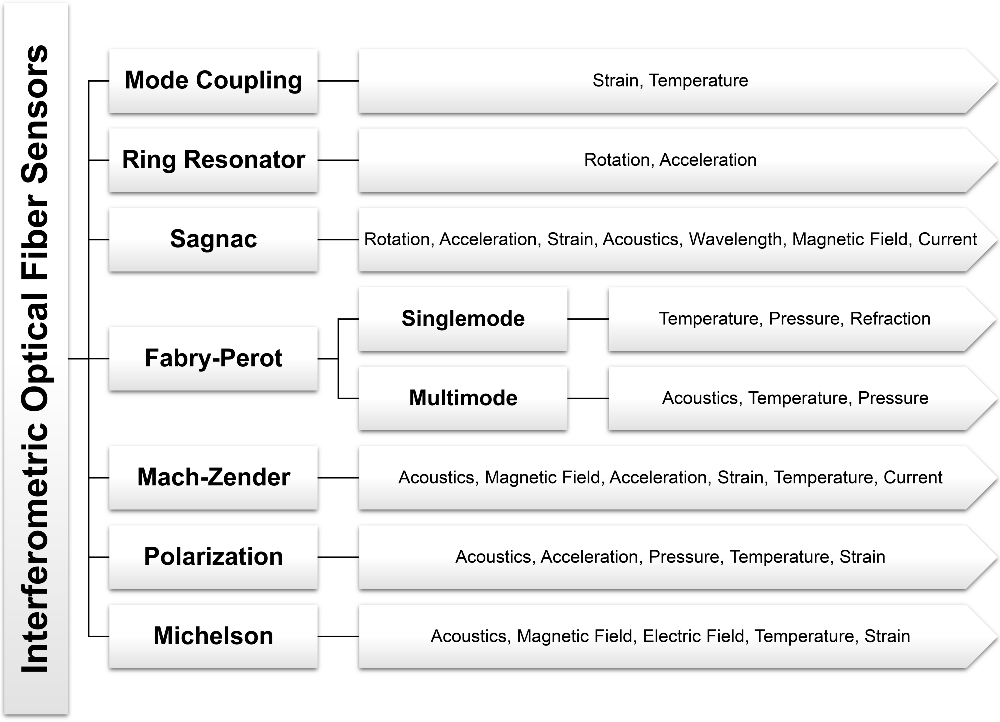

Figure 3.7 Interferometric optical fiber sensors.

MI sensors. Hence, MI sensors can be considered as half of MZI sensors in terms of configuration. The structure of SI based optical fiber sensors are more unique among other interferometric sensors. Incident light is splitted to counter propagate to each other in a loop, and measurements are done based on speed of the modes which are dependent on the polarization of the light beams [39]. FPI based sensors consists of two reflective surfaces separated from each other with a certain distance. Superimposition of light beams reflected from these surfaces creates an interference pattern. Even though there might be disadvantages resulting from manufacturing of FPI configurations which lowers the performance of the sensor, FPI sensors are the most preferable configuration among interferometric sensors because of cost effectiveness, stability, and high resolution [40].

4. THEORY

4.1 Principles of Fabry-Pérot Interferometry

Fabry-Pérot Interferometry is basically the superimposition of two light beams from perfectly aligned surfaces placed parallel to each other at a certain distance. The optical cavity consisting of these two reflecting surface acts as an interferometer and thus, such a device is known as a Fabry-Pérot Interferometer (FPI).

FPI fiber optic sensors are perfectly suitable for force, pressure, or strain measurements with low error ratio and high sensitivity. Some other sensing applications that can be achieved with FPI sensors, which might be useful for some applications in biomedical field especially in MRI guided interventions, can be summarized as follows [41]:

- Temperature Sensing
- Mechanical Vibration Sensing
- Acoustic Wave Sensing
- Ultrasound Sensing
- Voltage Sensing
- Magnetic Field Sensing
- Pressure Sensing
- Strain Sensing
- Flow Velocity Sensing
- Humidity Sensing
- Gas Sensing
- Liquid Level Sensing
- Refractive Index (RI) Sensing

FPI sensors are differentiated as intrinsic and extrinsic by whether the material is the same as the fiber (silica) between the reflective surfaces [42, 43].

For the prostate biopsy, the most suitable type of optical fiber sensing structure that can also be easily manufactured is an extrinsic Fabry-Pérot Interferometer design with a glass capillary covering the sensing cavity between the fiber endings. Glass capillary tube both conserve the fibers from the outside effects and works as a permanent fixation surface for the fibers.

A typical extrinsic FPI sensor is built upon a cavity with two cleaved fibers embedded in glass capillary as illustrated in Figure 4.1. The length of cavity between two fiber ends is in micrometer level and it varies accordingly with the needs of the application type. The incident light transmitted into first fiber reflects from the first fiber ending and also from the second fiber ending which is placed after the cavity. As a result, an interference pattern occurs with two light beams reflected from these surfaces. The interference pattern can be detected by using a beam splitter and photodiode.

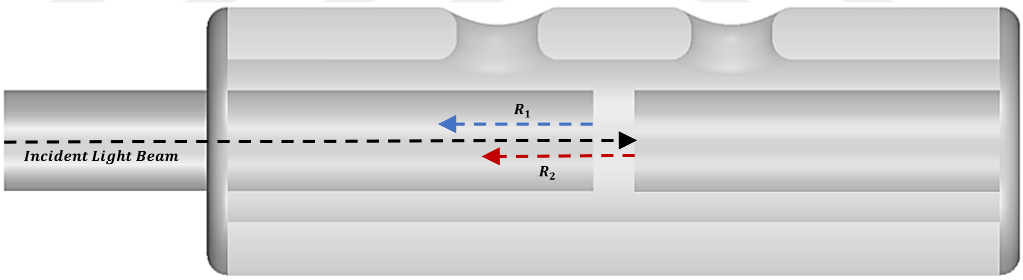

Figure 4.1 Working principle of Fabry-Pérot Interferometer.

The main idea behind extrinsic Fabry-Pérot interferometry-based fiber optic force sensors is creating an air cavity with a length dependent dynamic reflected light interference pattern based on the axial force applied on the sensor. The air cavity is formed between two partially reflective surfaces of two optical fiber ends. An interference pattern is created by reflected photons from the two surfaces, and the light intensity of reflected light is measured. The air cavity between two optical fibers changes with respect to the applied force at the sensor tip. A change in the air cavity means variations in the interference pattern formed by reflected lights and corresponds to a change at the light intensity that is being measured. Therefore, a linear relation is constructed between the force at the sensor tip and the measured reflected light intensity.

FPI is basically based on the superimposition of two light beams reflected from two reflective surfaces which are separated from each other at a dynamically changing distance. An incident light beam is emitted from a common light source. This light beam is separated into two beams as it passes through the reflecting surfaces. Reflected light beams follow the same trajectory with the same frequency. The reflecting surfaces in Fabry-Pérot Interferometry is characterized by their reflectance R_{FP} and transmittance T_{FP} can be defined as [44]:

$$R_{FP} = \frac{R_1 + R_2 + 2\sqrt{R_1 R_2}\cos\Phi}{1 + R_1 R_2 + 2\sqrt{R_1 R_2}\cos\Phi} \tag{4.1}$$

$$T_{FP} = \frac{T_1 T_2}{1 + R_1 R_2 + 2\sqrt{R_1 R_2}\cos\Phi} \tag{4.2}$$

where reflectance of reflective surfaces that construct FPI cavity are expressed as R_1 and R_2. R_{FP} represents the ratio of power of the reflected beam relative to power of the first light beam and T_{FP} represents the ratio of power of the transmitted beam relative to the power of the incoming light beam.

Φ is defined as the phase shift in FPI for a round-trip propagation of light beams. Φ is obtained as follows, considering $\pi/2$ phase shift occurs when light reflected from a surface [45]:

$$\Phi = \frac{4\pi n L}{\lambda} + \Phi_o \tag{4.3}$$

where n is the refractive index of the cavity material, n=1 for the designed FPI sensor since it is constructed with air cavity. It is noted that T_{FP} reaches its maximum when $\cos\Phi = -1$ or $\Phi = (2m+1)\pi$ where m is an integer.

Optical path difference (OPD) which describes a detuning phase of FPI cavity can be given as in 4.4 where n is the refractive index of the FPI cavity and L is the cavity length.

$$\Delta = 2nL \tag{4.4}$$

If total phase shift is defined as $\delta = \Phi - (2m+1)\pi$ and $\delta \ll 1$, T_{FP} approximates to its maximum value. In addition to that condition, if reflective surfaces of FPI cavity are assumed to be ideal with equal reflectivities close to unity, transmittance T_{FP} can be given as:

$$T = \frac{T^2}{(1-R)^2 + R\delta^2} \tag{4.5}$$

as it is assumed that $R = R_1 = R_2$, $T = T_1 = T_2$, and $T = 1 - R$. It can be observed from the above equations that T_{FP} is a periodic function of Φ with a period of 2π. Therefore, T_{FP} becomes half of its maximum value when:

$$\delta = \pm \frac{(1-R)}{\sqrt{R}} \tag{4.6}$$

This suggests that the finesse of FPI cavity, which is the ratio of the phase shift between subsequent transmittance peaks to the phase shift between half maximum points on the sides of transmittance peaks, can be given as [46]:

$$F = \frac{\pi\sqrt{R}}{(1-R)} \tag{4.7}$$

Reflectance R_{FP} of an ideal FPI with respect to phase shift is plotted in Figure 4.2. For FPI cavities with R≪1, the measure of finesse is not applicable since it is undefined for values of smaller than 0.172. When it is assumed again that FPI cavity consists of two surfaces of equal reflectivities and that value is very small, reflectance R_{FP} and transmittance T_{FP} can be simplified to the following:

$$R_{FP} \cong 2R(1 + \cos\Phi) \tag{4.8}$$

$$T_{FP} \cong 1 - 2R(1 + \cos\Phi) \tag{4.9}$$

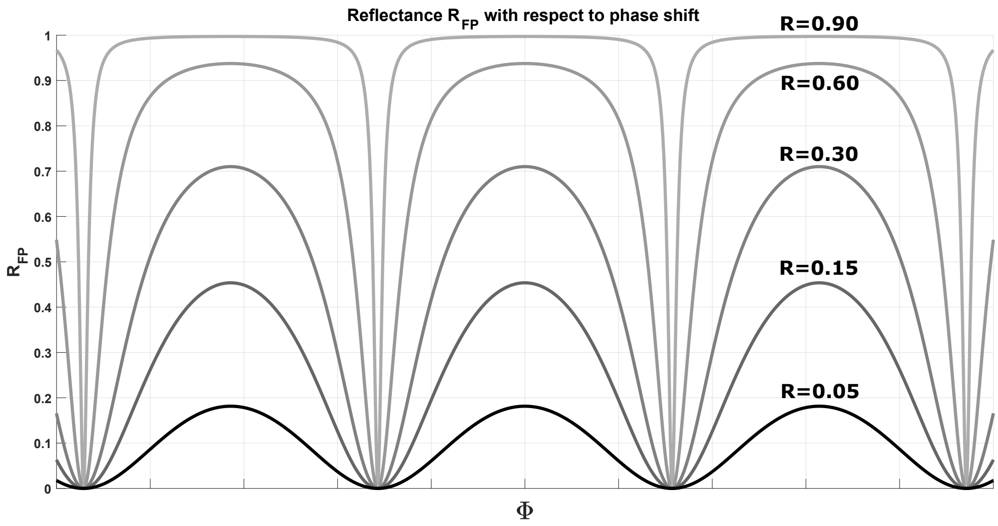

Figure 4.2 Ideal reflectance R_{FP} with respect to phase shift.

This approximation for reflectance R_{FP}, as seen in Figure 4.3, follows a closely similar pattern with the waveform of reflectance R_{FP} for R=0.05 in the expression 4.8.

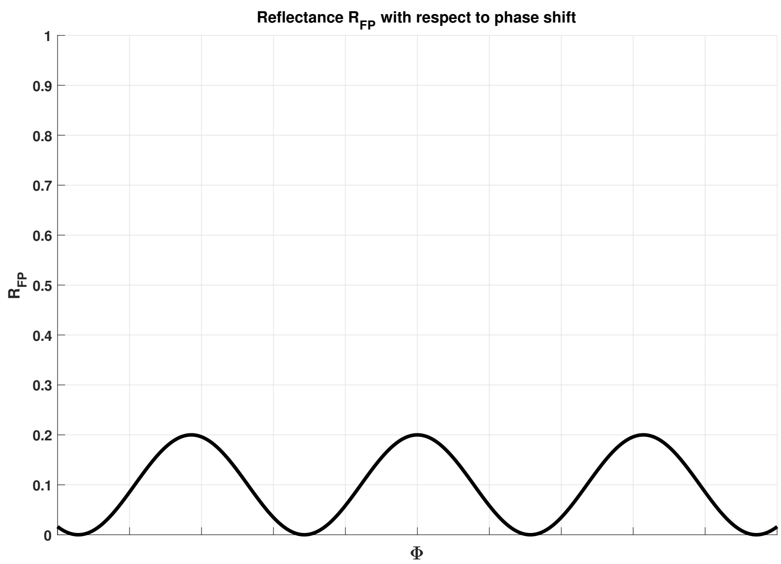

Figure 4.3 Reflectance R_{FP} with respect to phase shift.

Reflectance of common silica fiber is approximately 4% which is too low to provide successful reflection of multiple beams in FPI cavity [47]. According to Fresnel's equations of reflection, intensity of the reflected beams drops dramatically after the first two reflections. Therefore, light intensity from an FPI cavity constructed with optical fibers with low reflectance can be expressed with two of the reflected beams illustrated in Figure 4.4.

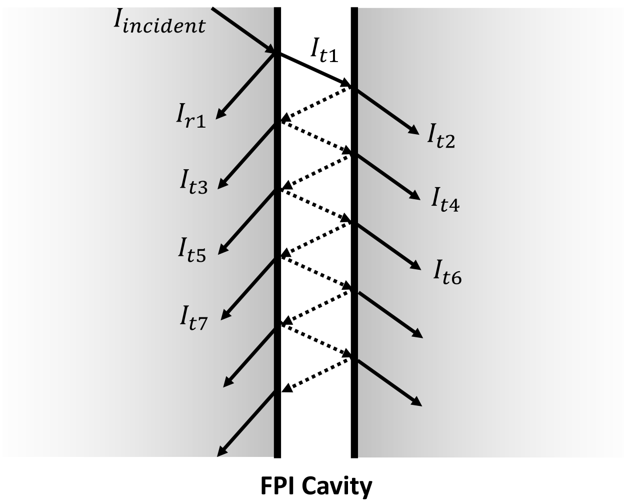

Figure 4.4 Reflections and transmissions in FPI cavity.

With this approximation, coherent addition of the first two reflection from the cavity with low reflectance gives the intensity of the reflected light coming from FPI sensor which can be seen in Figure 4.5.

Electric fields of the two reflective surfaces which are air-glass interfaces can be given as:

$$E_1 = A_1 \exp(j\Phi_1) \tag{4.10}$$

$$E_2 = A_2 \exp(j\Phi_2) \tag{4.11}$$

The amplitude of one of the electric fields reflected is expressed as [48]:

$$A_2 = A \left[\frac{ta}{a + 2\tan(\sin^{-1}(NA))L} \right] \tag{4.12}$$

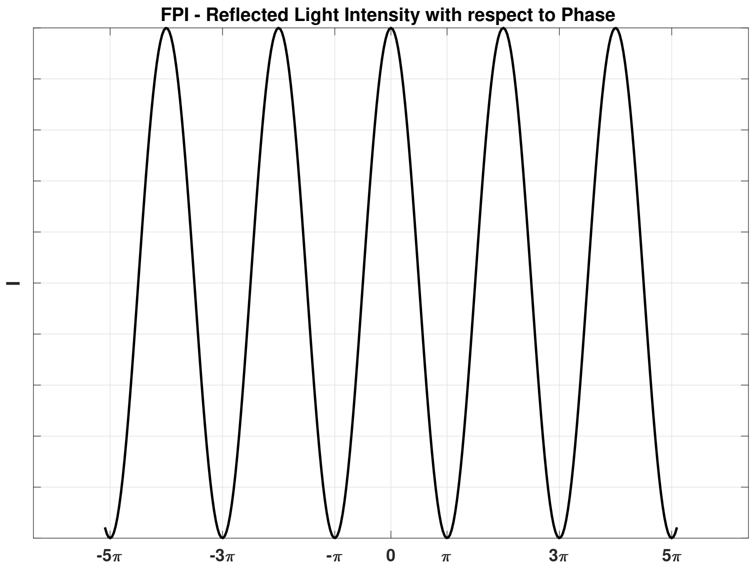

Figure 4.5 Reflected light intensity with respect to phase.

where t is approximately 0.98 which is transmission coefficient of air-glass interface, a is the fiber core radius, L is cavity length of FPI sensor.

Numerical aperture (NA) of the single mode fiber is calculated as $[NA = (n_1^2 - n_2^2)^{1/2}]$ where n_1 is refractive indix of the core, and n_2 is the refractive index of the cladding of the single mode fiber.

Based on the calculation of electric fields E_1 and E_2, the intensity of FPI interference can be found as follows:

$$I = |E_1 + E_2|^2 \tag{4.13}$$

$$I = A_1^2 + A_2^2 + 2A_1A_2\cos(\Phi_1 - \Phi_2) \tag{4.14}$$

and when $[I_1 = I_2 = I_0]$ the intensity of the interference simplifies to:

$$I = 2I_o(1 + \cos\Phi) = 4I_o\cos^2(\Phi/2) \tag{4.15}$$

Equation 4.15 can also be expressed based on the reflected light intensity from the second fiber given in equation 4.12 such that approximation for a real FPI cavity can be given as follows:

$$I = A^2 \left(1 + 2A_2 \cos(\frac{4\pi nL}{\lambda}) + A_2^2\right) \tag{4.16}$$

The total reflected light intensity from the FPI cavity is given Figure 4.6.

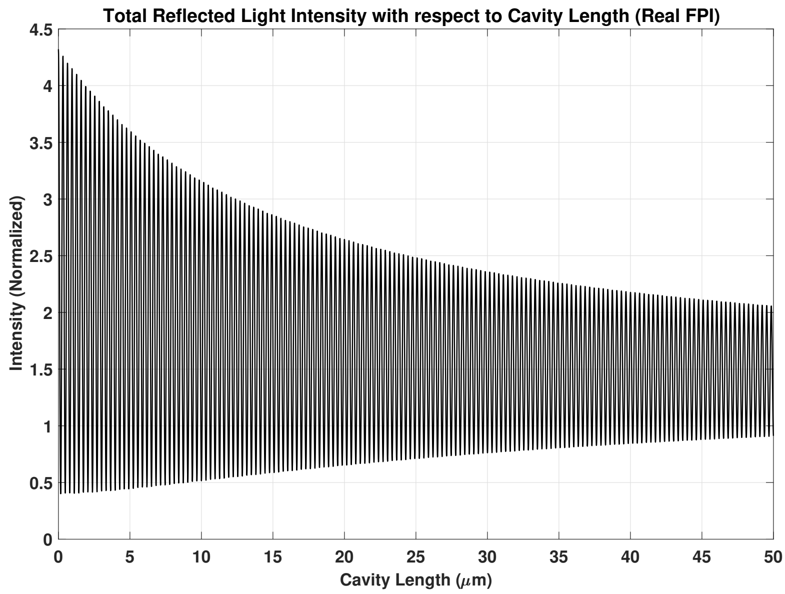

Figure 4.6 Total reflected light intensity with respect to cavity length (real FPI).

It can be clearly observed that fringe visibility decreases significantly with the increasing cavity length due to losses in the intensity of light reflected from the second fiber. For FPI sensing system with large cavities, the drop of fringe visibility drastically effects measurement resolution.

Based on the observations from Figure 4.6, it is critical to limit the FPI cavity to a small value in order to setup a sensing system with high resolution. The total light intensity for cavity lengths between 10 µm and 20 µm, which can be considered suitable for a high-resolution FPI system, can be seen in Figure 4.7. The resolution of the system drops drastically with increasing cavity length.

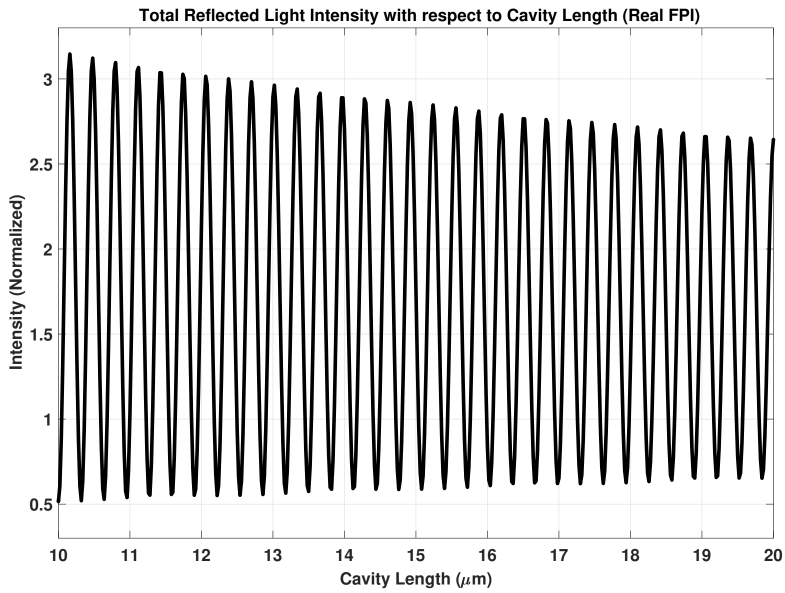

Figure 4.7 Total reflected light intensity with respect to cavity length (real FPI).

Figure 4.8 shows normalized reflected light intensity from the second fiber. It can be clearly observed that intensity of reflected light from second fiber is strictly dependent on the cavity length.

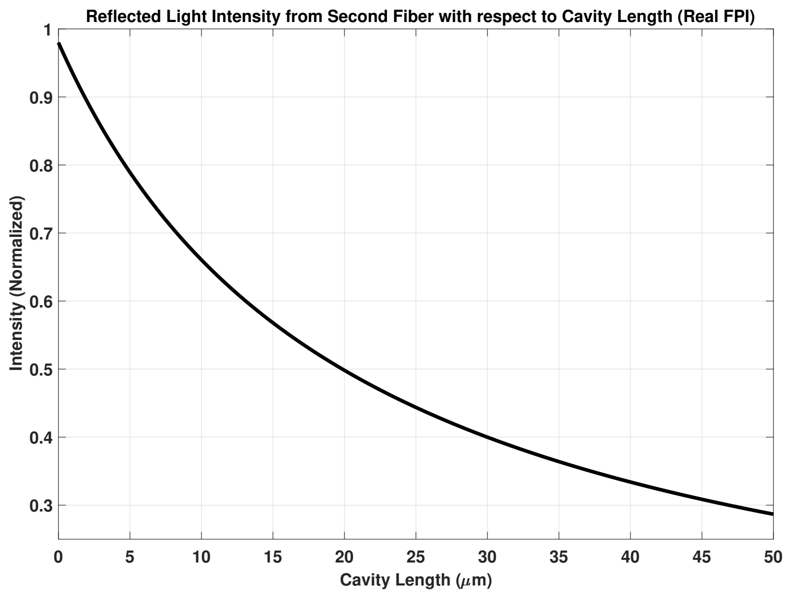

Figure 4.8 Reflected light intensity from second fiber with respect to cavity length (real FPI).

4.2 Measures of Performance for FPI Sensor

Some of the important factors that determine the performance of an FPI sensor are explained briefly below:

4.2.1 Q-Factor

Q-factor is the measure of the preserved energy in terms of light intensity in FPI cavity. It can be expressed as the ratio of power of the incoming light beam over energy losses per round-trip in FPI cavity.

4.2.2 Free Spectral Range (FSR)

Free spectral range (FSR) is the separation between two subsequent maxima or minima of reflected or transmitted light intensity in the interferometer in terms of wavelength, which is shown in Figure 4.9 [49].

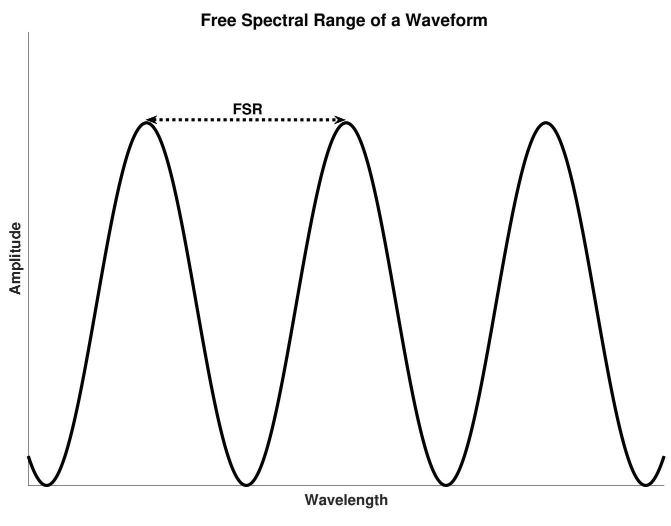

Figure 4.9 Free spectral range.

4.2.3 Finesse

Finesse is defined as fraction of free spectral range of the optical signal over its full-width at half-maximum (FWHM) [50]. Finesse is independent from cavity length but strictly dependent on the reflectivity of the materials used in the cavity. Finesse with respect to reflectivity can be seen in Figure 4.10

$$F = \frac{FSR}{FWHM} \tag{4.17}$$

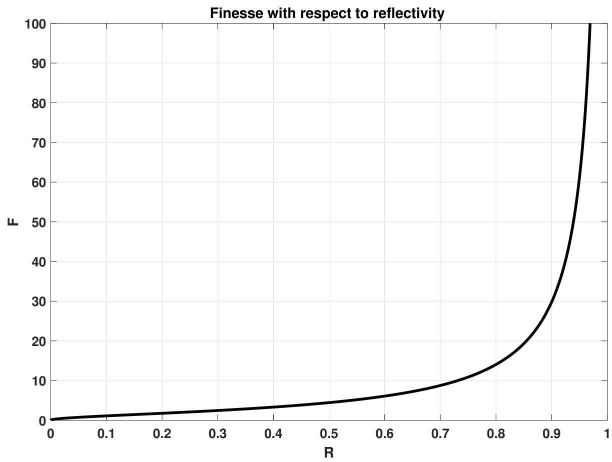

Figure 4.10 Finesse with respect to reflectivity.

4.2.4 Visibility

Fringe visibility quantifies the contrast of interference patterns based on observed maxima $I_{\max}$ and minima $I_{\min}$ of intensity of the reflected light beams:

$$\nu = \frac{I_{\max} - I_{\min}}{I_{\max} + I_{\min}} \tag{4.18}$$

4.3 Process Control Theories

4.3.1 Model Predictive Control (MPC)

The main principle behind MPC is finite-horizon optimization of a dynamic system based on iterations. With structure shown in Figure 4.11, cost minimizing control strategies that will be effective in a predefined time horizon are created for every iteration of time.

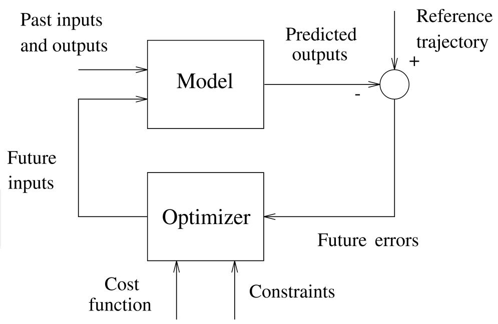

Figure 4.11 Structure of Model Predictive Control (MPC).

Only the first step of this control strategy is implemented to the system, and then calculations for new control strategies are repeated based on the new current state. Hence, the prediction horizon shifts after each control implementation, which makes MPC a receding horizon control approach. The working principle of MPC model is illustrated in Figure 4.12:

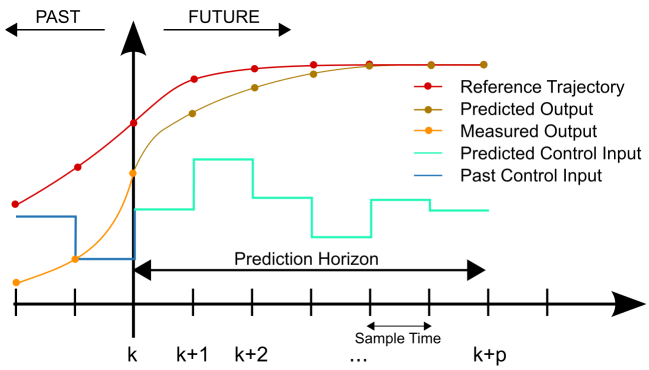

Figure 4.12 Working principle of Model Predictive Control (MPC).

The prediction based control model with single-input and single-output can be explained with state space model as follows [51]:

$$\begin{aligned}
\begin{pmatrix} x(t+1) \\ u(t) \end{pmatrix} &= \begin{pmatrix} A & B \\ 0 & I \end{pmatrix} \begin{pmatrix} x(t) \\ u(t-1) \end{pmatrix} + \begin{pmatrix} B \\ I \end{pmatrix} \Delta u(t) \\
y(t) &= \begin{pmatrix} C & 0 \end{pmatrix} \begin{pmatrix} x(t) \\ u(t-1) \end{pmatrix}
\end{aligned} \tag{4.19}$$

Process dynamics can be summarized as:

$$\begin{aligned}
x(t+1) &= Ax(t) + Bu(t) \\
y(t) &= Cx(t)
\end{aligned} \tag{4.20}$$

If the new state vector is defined as:

$$\bar{x}(t) = \begin{pmatrix} x(t) & u(t-1) \end{pmatrix}^T \tag{4.21}$$

The model in 4.3.1 takes a general incremental form:

$$\begin{aligned}
\bar{x}(t+1) &= M\bar{x}(t) + N\Delta U(t) \\
y(t) &= Q\bar{x}(t)
\end{aligned} \tag{4.22}$$

4.3.2 PID Control

Proportional integral derivative (PID) is a system of a control with a feedback loop. PID takes past-present-future errors into account as proportional controller focuses on the present errors, integral controller calculates the build-up of the past errors, and derivative controller makes prediction of future errors.

Three components of PID controller are expressed as follows:

- Proportional term gives an output depending on the values of the current error. With proportional control, output of the control system changes based on multiplication of current error with the proportion defined by the constant K_p as expressed in 4.3.2.

$$P = K_p.error(t) \tag{4.23}$$

- Integral term takes accumulation of error into account depending on the term K_i as expressed in 4.3.2. It minimizes steady-state error of the system with the trade off an overshoot.

$$I = K_i \int_0^t error(t)dt \tag{4.24}$$

- Derivative term is defined as multiplication of the term K_d and the slope of the error as given in 4.3.2:

$$D = K_d \frac{d(error(t))}{dt} \tag{4.25}$$

Block diagram of basic PID controller is shown in Figure 4.13:

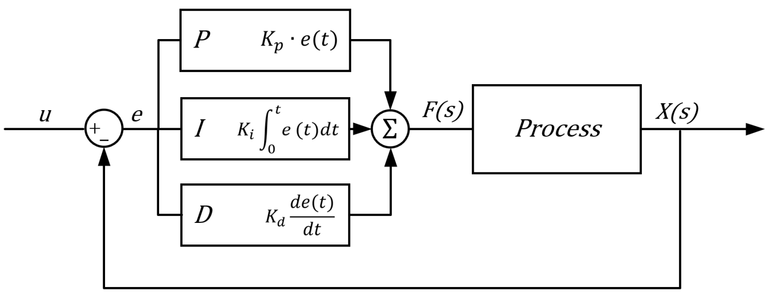

Figure 4.13 Block diagram of PID controller.

The overall transfer function G(s) of PID controller is given as:

$$G(s) = \frac{U(s)}{E(s)} \tag{4.26}$$

$$G(s) = K_P + \frac{K_I}{s} + K_D s = \frac{K_D s^2 + K_D s + K_I}{s} \tag{4.27}$$

Response of closed-loop PID controller depending on variations of K_p, K_i, and K_d is summarized in Figure 4.14 below:

Parameter	Rise Time	Overshoot	Settling Time	Steady-State Error
K_p	Decrease	Increase	Small Change	Decrease
K_i	Decrease	Increase	Increase	Significant Decrease
K_d	Minor Decrease	Minor Decrease	Minor Decrease	No Effect in Theory

Figure 4.14 Effects of PID Parameters.

For tuning of PID control parameters, Ziegler-Nichols method is the most convenient choice. Derivative gains are set to zero initially. Proportional gains are increased until the system output starts oscillations. The gain at which the system starts oscillating K_u and the period of oscillations T_u are used to calculate K_p, K_i, and K_d according to the Figure 4.15.

Control Type	K_p	K_i	K_d
P	$K_u/2$	-	-
PI	$K_u/2.2$	$1.2K_p/T_u$	-
PID	$0.6K_u$	$2K_p/T_u$	$K_pT_u/8$
Some Overshoot	$0.33K_u$	$2K_p/T_u$	$K_pT_u/3$
No Overshoot	$0.2K_u$	$2K_p/T_u$	$K_pT_u/3$

Figure 4.15 P,I,D calculations based on Ziegler-Nichols method.

5. METHODS

In this section, design and fabrication of a fiber optic force sensor based on FPI at the tip of an 18-gauge prostate biopsy needle is presented. Entire setup of FPI force sensing system is shown in Figure 5.1.

The sensor was built upon an air cavity between two cleaved optical fibers with a diameter of 125 μm which were embedded and fixed into a borosilicate glass capillary with an inner diameter of 200 μm. Fixation of optical fibers within the glass capillary were achieved by applying medical grade UV adhesives through two micro-holes formed with CO_2 laser processing on the glass capillary. The initial distance between the fiber endings was adjusted by using manipulators controlled by piezoelectric actuators and strain gauge readers with a resolution of 10 nm. A laser diode which has a wavelength of 635 nm was used as the light source for the operation of the sensor.

The intensity from the laser diode was kept constant during operation with custom-made current feedback mechanisms and temperature controllers. Model predictive control approaches were adapted and implemented for the temperature control of the light source. A circuitry for the operational control of the system and signal processing was implemented. The sensor was calibrated and optimized by using a commercial pressure sensor and a force testing machine. Dynamic range of the sensor was set to the linear operation region to avoid signal ambiguity while being able to provide a force measurement range of 0-13 N with a resolution of 0.1 N based on in vitro needle insertion experiments.

Being small, compact and immune to EMI and RFI are considered as main criteria while designing FPI sensors which are suitable for interventional MRI devices. Force measurement at the needle tip during prostate biopsy under MRI, which is the main objective of the project, can be performed by using the custom designed FPI based fiber optic sensor with desired force range and resolution.

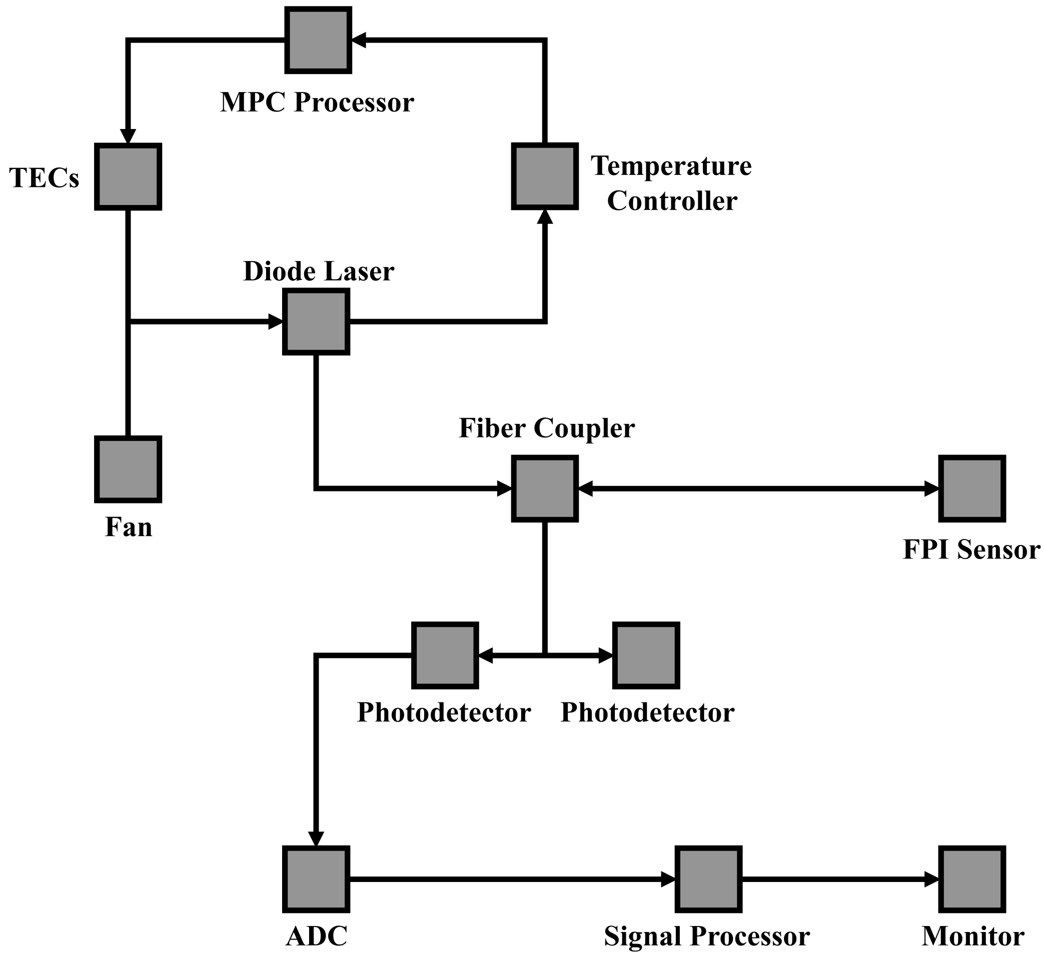

Figure 5.1 FPI force sensing system.

5.1 Optical Setup

Optical circuit setup consists of a laser driver, laser diode, photodiode for feedback, beam splitter, FPI force sensor, signal processing system, which are shown in Figure 5.2. The light beam from the laser diode was transmitted to FPI force sensor through optic fibers of which core diameter is 3.5 μm and cladding diameter is 125 μm.

Setup of the optical circuit include the following elements:

- Laser Source: 8mW, 635nm laser diode
- Laser Driver: Voltage regulator circuit
- Beam Splitter: 45:55 splitter

- Collimator: 1 at the laser output, 1 at the splitter output
- Optical Fixture
- Fiber Ending
- Fiber Connector
- Optical Fiber
    - 5 μm core, 125 μm cladding, single mode fiber
    - 400 μm core,430 μm cladding, multi-mode fiber
    - 600 μm core, 630 μm cladding, multi-mode fiber
- Photodetector: Adjustable (PDA36A-EC, Thorlabs Inc.)

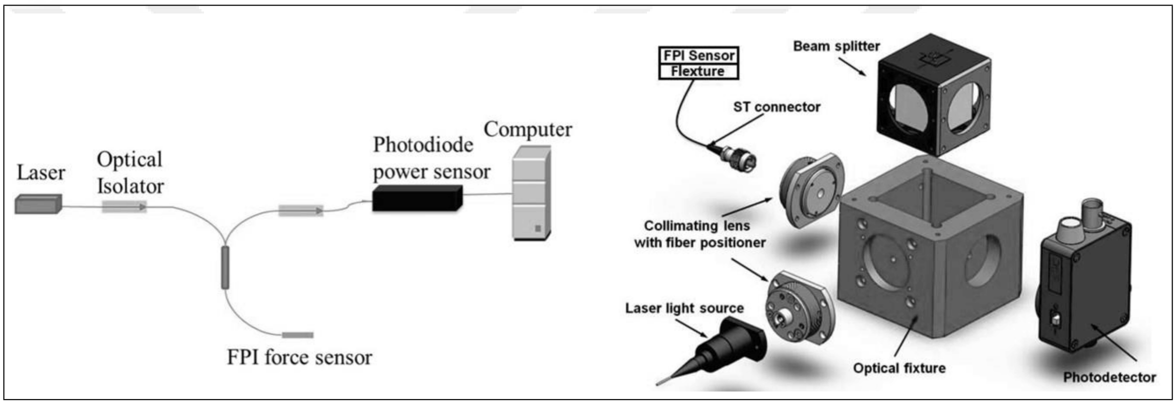

Figure 5.2 Optical setup.

5.2 Sensor Design

The sensor was built upon an air cavity between two split optical fibers with a diameter of 125 μm which were embedded and fixed into a borosilicate glass capillary of which inner diameter is 200 μm as illustrated in Figure 5.3. The outer diameter of the glass capillary is 300 μm, and it has a length of 2 mm. The sensing part which can be described with the gauge length of the sensor constitutes a small portion of the glass capillary. Therefore, the length of the sensor can be minimized further if needed. The sensor structure provides a robust and miniature configuration with these dimensional specifications. It can be embedded at the tip of a biopsy needle without causing any significant obstructions.

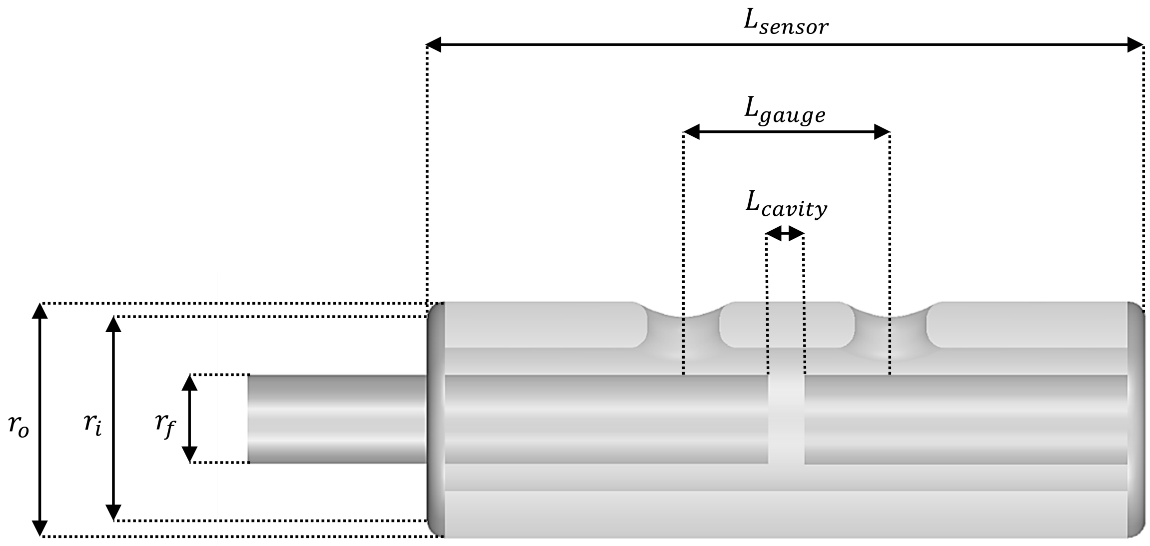

Figure 5.3 FPI sensor dimensions.

The gauge length of the sensor is the most critical dimensional factor which determines the sensitivity of the sensor for force measurement [52]. The air cavity between cleaved optical fibers together with the gauge length as the effective length changes when an axial force is introduced on the sensor. As long as the glass capillary remains uniform along its axis, the relation between the applied pressure and the change in cavity length can be given as [53, 54, 55, 56, 57]:

$$\Delta L_{cavity} = \frac{(L_{gauge})}{E\pi(r_o^2 - r_i^2)}(1 - 2\mu)F$$

which shows that the change in cavity length (ΔL_{cavity}) has a linear relation with the amount of force applied (F). Young's modulus (E), and Poisson's ratio (μ) are important factors to consider when choosing the sensor material. Effective gauge length (L_{gauge}), inner radius (r_i), and outer radius (r_o) should be determined based on the aimed range of force measurement.

Effective gauge length can be defined with high precision by changing the po-

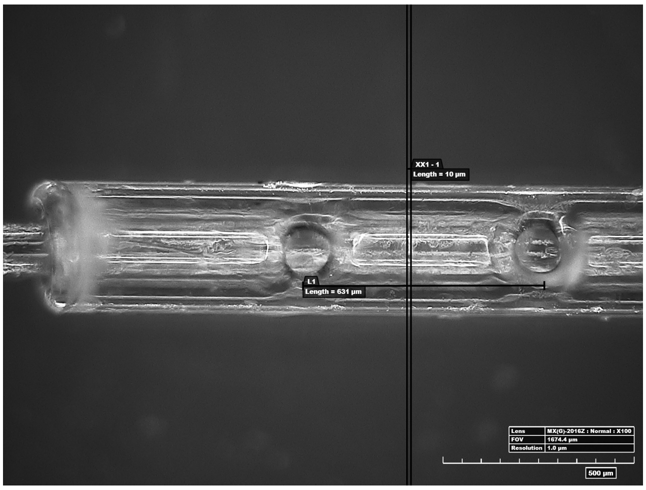

Figure 5.4 Manufactured FPI sensor.

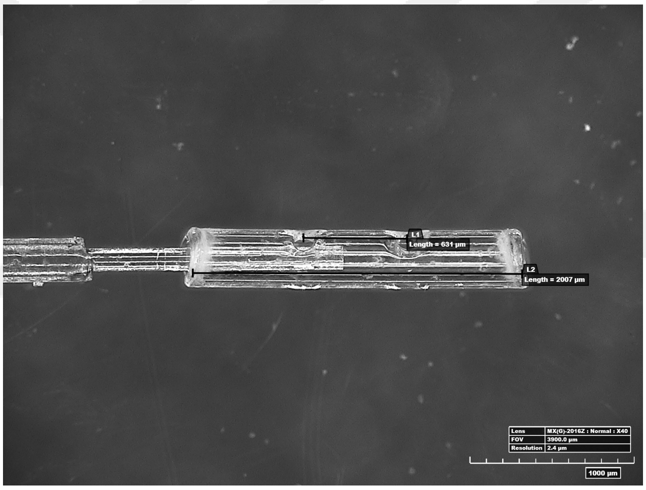

Figure 5.5 Manufactured FPI sensor.

sition of micro-holes from which UV adhesives are applied to fix the fibers within the glass capillary. UV adhesives were applied to a particular region with the flexibility provided by the micro-holes. The custom made FPI sensor that can be seen in Figure 5.6 is novel in terms of that flexibility to arrange gauge length during the fabrication process.

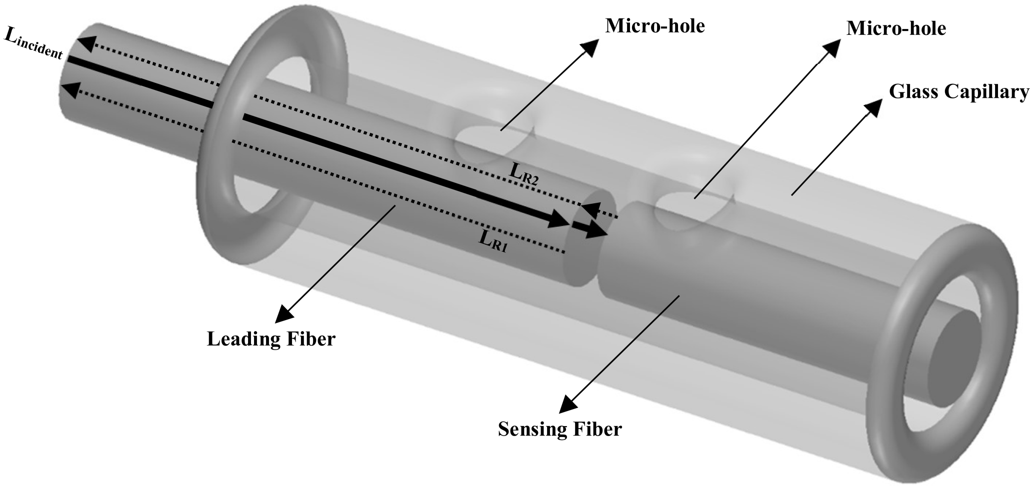

Figure 5.6 FPI sensor structure.

5.3 Materials

Borosilicate glass capillary was chosen to form the sensor since it outperforms among other glass compositions in terms of mechanical, thermal, and chemical properties. Borosilicate glass has chemical inertness to a large variety of materials, which makes it medically safe to use in biopsy interventions. The sensor encapsulated in borosilicate glass is expected to have an excellent chemical durability and corrosion resistance. Another important advantage of using borosilicate is that it has a very low thermal expansion coefficient compared to other glass composites. Hence, cross sensitivity due to thermal expansion on the structure of the sensor during the needle insertion is minimized. A large tensile strength that enables force measurements up to 13 N is also achievable even though wall thickness of the borosilicate glass capillary is small.

5.4 Fabrication Methods

Despite its unique and outperforming properties, brittleness and hardness of the borosilicate glass cause a challenge for the micro processing of the borosilicate glass tubes. As a cost effective and practical method mechanical processing was tested on glass capillaries. It was observed that mechanical processing methods require some further optimization to avoid cracks on the glass capillaries and to increase precision of the application. Therefore, CO_2 laser, which provides high precision and flexibility together with cost-effectiveness was preferred for micro processing of borosilicate glass capillaries. As seen in Figure 5.7, precise cutting of glass capillaries with a length of 2 mm and drilling of micro-holes with a diameter of approximately 50 μm were achieved by using 60W CO_2 laser (Epilog Legend Series, Epilog Laser). The engraving system

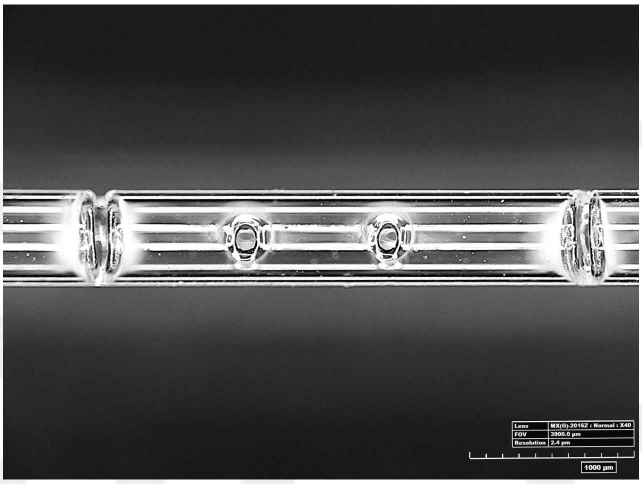

Figure 5.7 Laser processed borosilicate glass capillary.

used for glass processing prevented formation of debris around the cutting edges and micro-holes, which is a common problem. Even though CO_2 laser processing is precise and powerful, transferring the required energy through borosilicate glass for drilling and cutting is a difficult task since borosilicate glass is transparent to a wide range of wavelengths. Therefore, the transmission rate of borosilicate glass capillaries was increased by filling with water which reduces reflection losses at the inner surface. Processing of borosilicate glass capillaries was optimized by this final improvement.

After laser processing of borosilicate glass capillary, the alignment and fixation of two optical fibers were done with the consideration of obtaining a sufficient signal-to-noise-ratio (SNR) for measuring the axial force with a desirable resolution. Integration of the parts of the EFPI sensor was made on an optic table which provides vibration isolation.

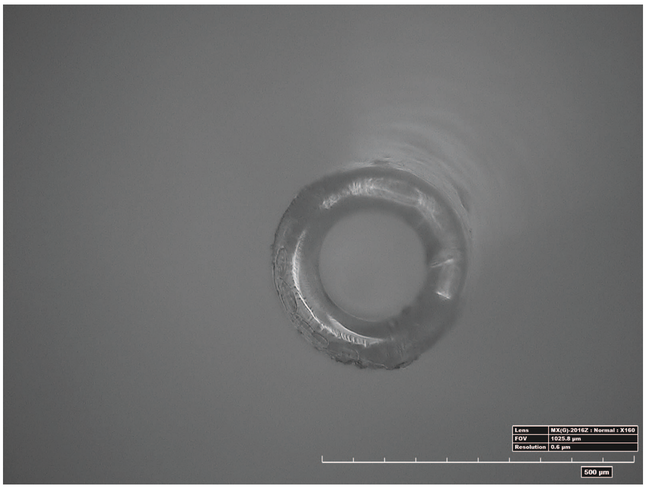

Figure 5.8 Laser processed borosilicate glass capillary (axial view).

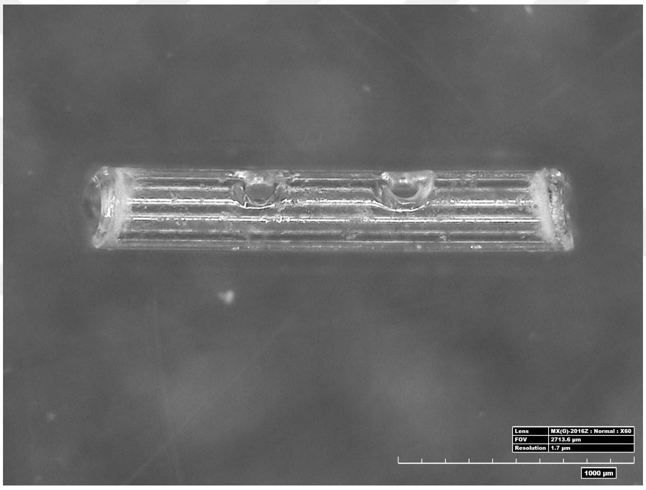

Figure 5.9 Laser processed borosilicate glass capillary (lateral view).

As a first step for the integration, the borosilicate glass capillary was fixed onto a three-stage manual micro manipulator. The glass capillary was then aligned in such a way that the micro holes previously formed on it looks up, enabling medical grade UV adhesive application through micro-holes. The leading fiber was placed and fixed onto a piezoelectrically driven stage which was in front of the manual micromanipulator as shown in Figure 5.10. The leading fiber was moved into the glass capillary by using micro manipulator and the piezoelectric actuators while the two parts were visually inspected with the help of a microscope. After applying UV adhesives to the glass capillary and the fiber, UV exposure was applied throughout borosilicate glass which is transparent to UV light. The same process was repeated for the integration of the

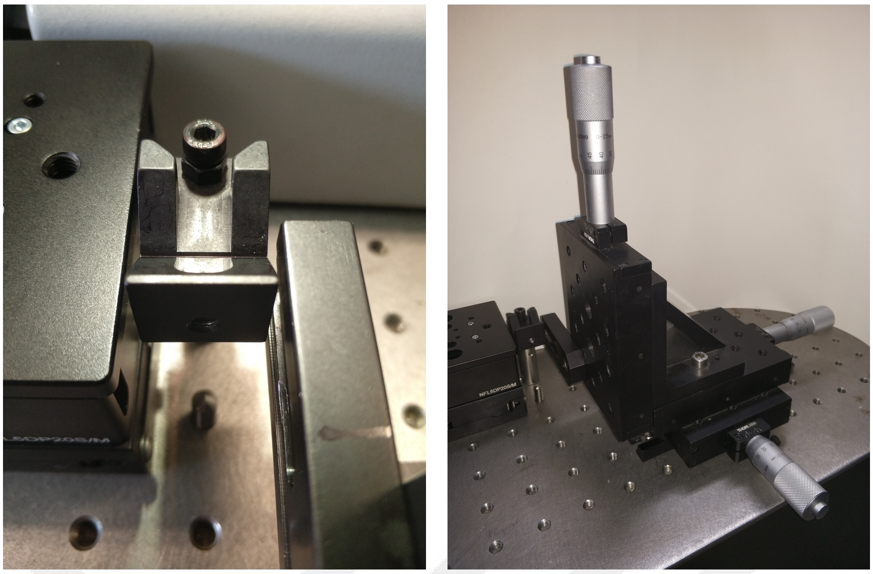

Figure 5.10 Setup for integration of the sensor parts.

ending fiber, which completed the fabrication of the EFPI sensor.

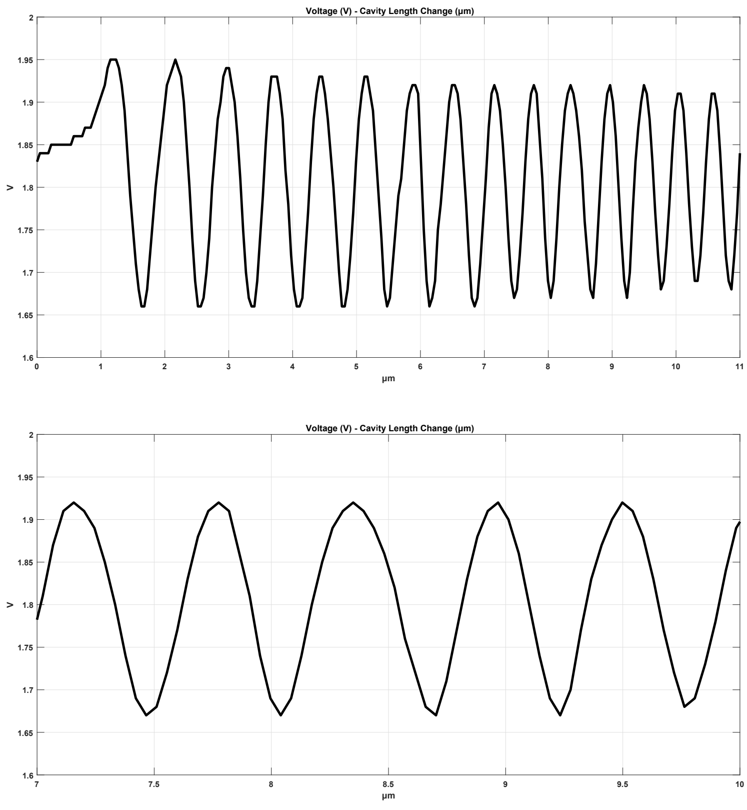

Figure 5.11 Linear response of FPI sensor.

Alignment of the fibers endings in the glass capillary was done based on the maximum feedback signal intensity for different orientations and optimal cavity distance for precise force sensing for the measurement range specified as 0-13 N with a resolution of 0.1N. The typical response of the sensor during adjustment and alignment of the sensor parts is given in Figure 5.11. Temperature compensation was also achievable by adjusting the air cavity distance between the two fibers based on the thermal expansion coefficients and the structure of the sensor. As seen in Figure 5.12, the sensor

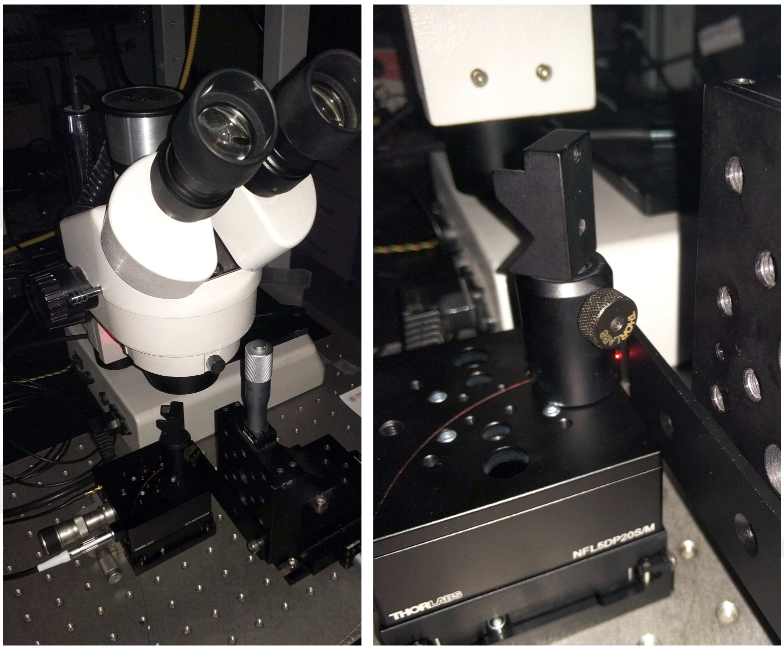

Figure 5.12 Integration setup with microscopic visualization.

was visually inspected under a microscope during the entire integration process. Eventually, the performance of the fabricated sensor was optimized by adjusting the gauge length precisely with piezoelectric actuated nano positioning stage (NFL5DP20S/M - NanoFlex, Thorlabs, Inc.). The working range of the sensor was set to the linear region of the signal that forms interference patterns based on reflected light beams.

5.5 Calibration of the Sensor

The sensor was calibrated with a material force testing machine (LF-Plus, Lloyd Instruments Ltd.) seen in Figure 5.13 so that it has a range of 0-13 N and 0.1 N resolution. The capability of the sensor for measuring forces up to 20 N was tested by

Figure 5.13 Force calibration setup.

increasing the applied force with small increments. Calibration force measurements up to 5N are given below in Figure 5.14.

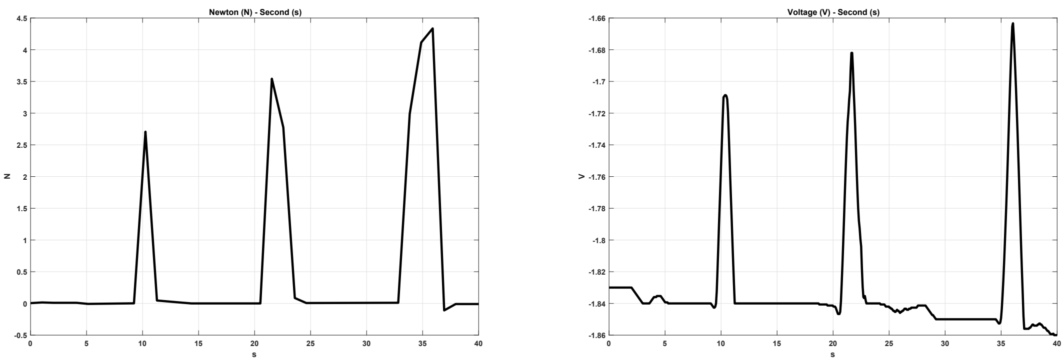

Figure 5.14 Force calibration measurements.

5.6 Force Range of the Sensor

The reliability of EFPI design was verified for axial force measurement with a range of 13 N which is higher than the average axial force exposed during typical prostate interventions [58]. Needle insertion force analyses on normal and cancerous prostate tissues shows that axial force occurred during the insertion do not exceed

15 N [59]. Force profiles acquired during needle insertion into prostate indicates the maximum force is measured at the beginning of the insertion and it is about 14 N [60]. The applied force on the tissue reaches its maximum during the puncture of the perineum wall. Other in-vivo data from a total of 72 prostate interventions of 25 patients in operating room includes an average maximum force of 16.7 N for one of the patients, and the average maximum force of all insertion of all patients is about 10 N [61]. Therefore, it can be concluded that the EFPI sensor design with a measurement range of 13 N can be used for prostate interventions to acquire average force data.

The FPI design was able to provide axial force measurement up to 13 N which is higher than the average axial force exposed during typical prostate interventions [58, 59, 60, 61]. During the sensor fabrication, the gauge length was arranged with high precision based on the force measurement range needed for prostate biopsy interventions.

5.7 Signal Processing System

For measurement applications, MSP430F5529 meets the needs with its microcontrollers and several peripheral sets. The efficient and cost effective board was optimized for signal processing for both temperature control of the laser and signal acquisition from the sensor designed.

MSP430F5529 LaunchPad electronic board seen in Figure 5.15 was used for all of the signal processing tasks including interpreting data from the force sensor and temperature sensors. In addition to that, any temperature or force control algorithms were implemented on the MSP430F5529 board.

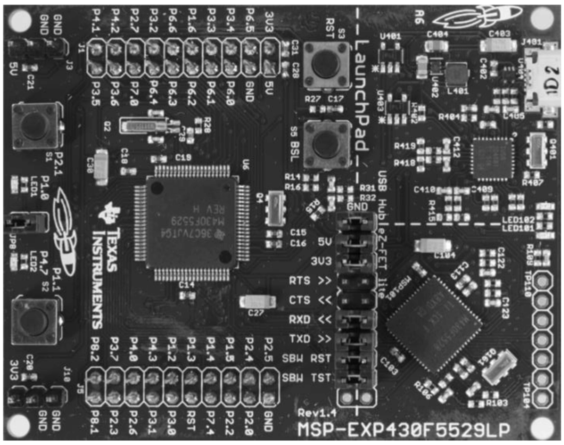

Figure 5.15 MSP430F5529 Launchpad Board.

5.8 Temperature Controller for Laser Source

A laser diode which has a wavelength of 635 nm was used as the light source for the operation of the sensor. Force measurements were done by based on the interference patterns formed. It is critical to consider effects of temperature change on the operation parameters of the laser since it is a known fact that current threshold which is one of the main characteristics of a laser source is highly dependent on the ambient temperature [62, 63]. Such variations in the main characteristics of a laser result in shifts in bandwidth and wavelength of the beam emitted from the laser [64, 65]. The rate of motion of positive and negative charges in PN junction increases significantly when temperature increases. As a result, emission power and light intensity induced from laser falls dramatically.

It is required to set a temperature value for the operation of the laser and keep that temperature constant in case of any outside effects in order to achieve accurate interferometric measurements. Thorlabs LP635-SF8 laser used in the project includes a photodiode for the control of laser current and power. However, this feedback mechanism is insufficient to prevent effects of temperature changes on the laser operation. Hence, a dedicated temperature controller for laser source was implemented so that the intensity from the laser diode was kept constant during the operation. Model predictive control approaches were adapted and implemented for the temperature control of the laser source.

Model Predictive Control (MPC) is an approach that combines multiple methods to obtain an optimal control output. There are a variety of MPC algorithms which differs in terms of definition of a model for the control system and minimization of the objective functions. However, the main principle behind all MPC approaches is use of a model to predict future outputs of the system and minimizing the difference between predictions and desired trajectory. The future outputs are calculated for a pre-defined prediction horizon with a specified range which shifts a step after the first control step within the horizon is determined [51]. Hence, MPC can be described as a receding horizon control approach. Even though control approach is easy to implement, derivation of the prediction trajectory for every sampling time causes a computationally higher cost compared to classical control methods such as PID [66]. This computational cost does not cause a fundamental problem when a processing system with adequate processing power is used.

A heat sink made of Aluminum (Al) was designed based on the dimensions and the shape of the laser source. Multiple temperature sensors that were placed in that Al housing also give information about the distribution of heat coming from the laser source.

Temperature measurements were done by using DS18B20 (Maxim Integrated) digital sensors. Digital temperature data was transmitted to MSP430F5529 LaunchPad (Texas Instruments Inc.) electronic board, and those were used as the input for control algorithm created with Matlab MPC toolbox and transferred to the electronic board [67]. MPC setup for temperature control of laser source, which was created in Matlab Simulink environment, can be seen in Figure 5.16. Thermoelectric Coolers (TECs) which were integrated onto the Al housing were fed with a current that variates based on the output of the control algorithm constantly running on the electronic board. TECs consist of two different layers of semiconductors which behaves as n-type and p-type, and when a DC voltage is applied a heat flux is created between two layers as seen in Figure 5.17 [68]. Such a temperature control system required also the use of

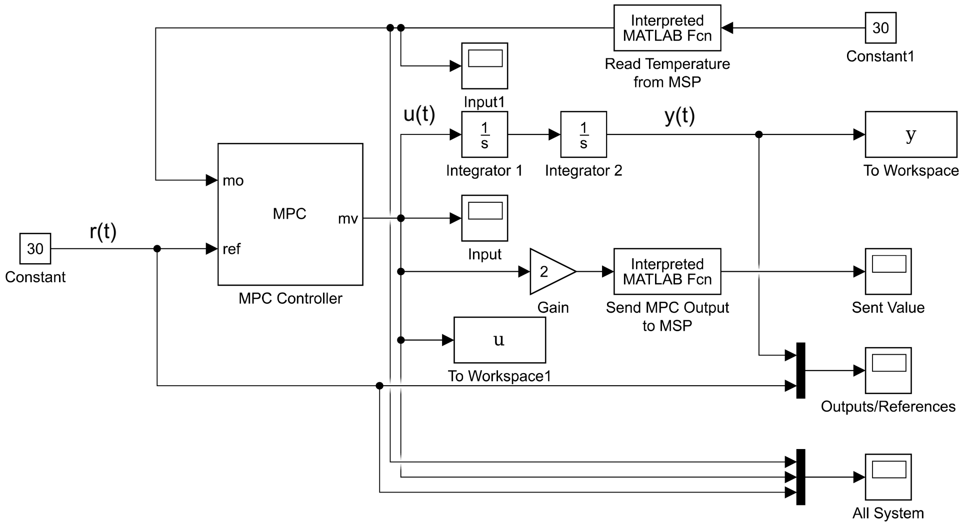

Figure 5.16 MPC setup for temperature control.

some powerful fans to create air flow around the housing and send out the excess heat around the laser source [69].

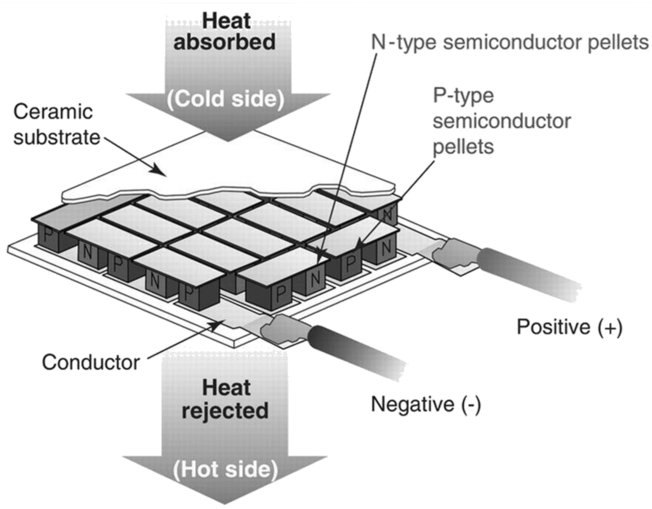

Figure 5.17 Operation principle of TECs.

Temperature change has also some other dramatic effects on the laser operation in terms of safety. Instant falls in the laser output prolong the time needed for laser material to radiate, and it can even shut out that process [70]. As a result of that, there is a high possibility of burning of the inner material and expected damage to the laser source together with connected parts will probably occur. Therefore, a temperature control system for laser source is also essential for the safe operation of the optical system of the force sensor.

Temperature control system for the laser source includes the following elements:

- Aluminum Housing
- TI MSP430F5529 LaunchPad
- Thermoelectric Coolers (TECs)

The system was operated with PID and MPC approaches and these two control methods were compared in terms of their performance. The most important factors considered in this comparison were the ability of the system to maintain the desired temperature against external influences, and the consistency of the system responses to reach the target temperature. In a scenario created for the comparison of PID and

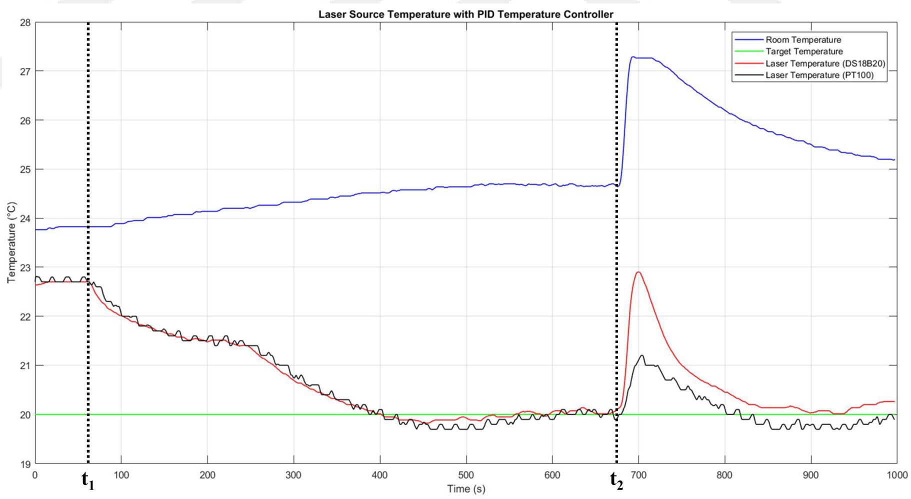

Figure 5.18 PID based temperature control under excess heat exposure.

MPC control approaches under the same ambient conditions, the temperature of the laser source was intended to be lowered to 20 °C where the room temperature was 24 °C. Systems were activated at time t_1, the performance of two control approaches were observed with both digital and analog temperature sensors. While the MPC-based temperature control system reached this temperature target in less than 250 seconds, it took up to 600 seconds for the PID-based system to reach this temperature and

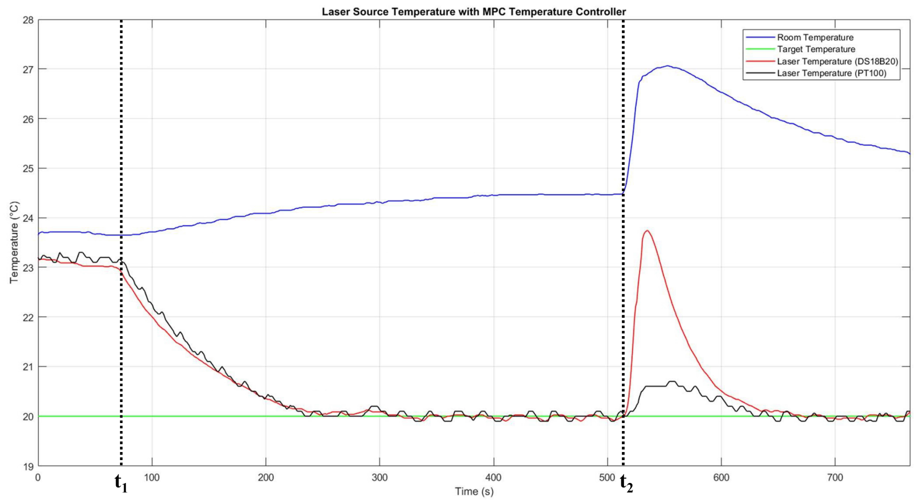

Figure 5.19 MPC based temperature control under excess heat exposure.

maintain the target temperature. Then, the laser source was voluntarily exposed to an excessive heat after time t_2 for a short time.

In this way, MPC and PID control mechanisms were tested for their preventive responses. It was observed that the temperature control system based on MPC approach reacted to the outside effects more robustly and consistently compared to PID, which can be seen in Figure 5.18 and Figure 5.19. Hence, the laser source of which temperature was controlled by MPC reaches the target temperature in a shorter time after an exposure of heat.

It was observed that the temperature control system operated by the MPC approach has a fast response to reach target temperature and the target temperature can be maintained for a long time even if there are changes in the ambient temperature. As seen in Figure 5.20, temperature fluctuations of only 0.06 °C occurred at the measured temperature at the laser source. These fluctuations do not reduce the operating performance of the laser source and there are no adverse effect on force measurements.

At the FPI sensing side, some temperature effect might also occur even though

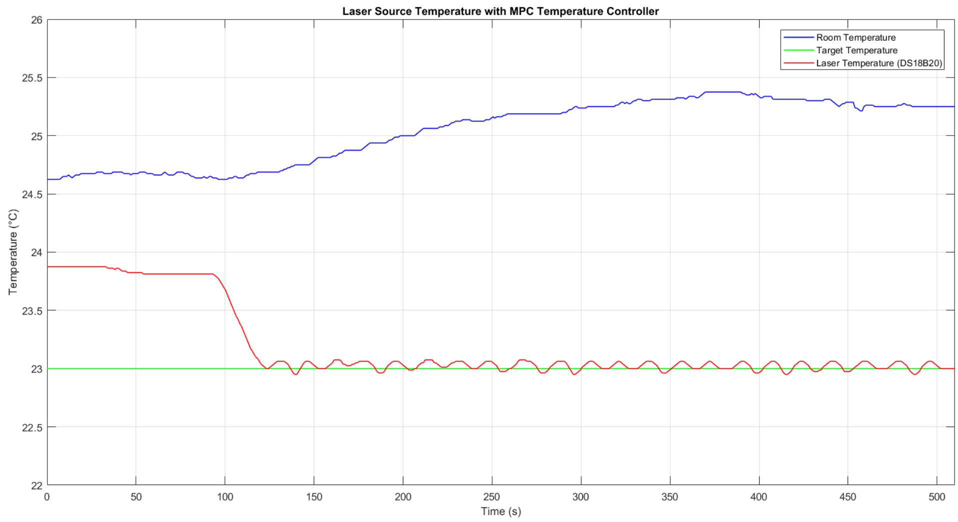

Figure 5.20 MPC based temperature control of the laser source.

such an effect is eliminated by the expansion of the glass capillary itself, which requires to take temperature compensation into consideration for a few micrometers. Among other optical force sensing technologies, Fabry-Pérot force sensors are significantly less thermally sensitive. However, effect of temperature on the sensing mechanism of the sensor should be eliminated for reliable data during prostate biopsy. This can be achieved by the integration of another FPI sensor onto biopsy needle in order to measure the effects of temperature to signal feedback [71].

6. RESULTS

6.1 Manufactured FPI Force Sensor

Fiber optic based FPI force sensors were developed by following the manufacturing procedures explained in detail in the previous sections, and in [72]. Even though manufacturing procedures have been optimized during the project, performance of the sensors designed might differ from each other due to small variations of some parameters that define main characteristics of the sensors. A representative microscopic image of the manufactured sensors is given in Figure 6.1.

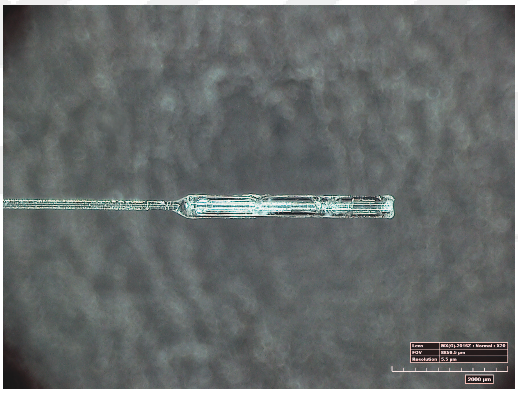

Figure 6.1 Example of manufactured FPI sensor.

Specifications of the sensors are summarized in Table 6.1. Specifications such as force measurement range and resolution can be changed precisely according to the specific needs of an application during which the sensor will be used.

6.2 Preliminary Results

The response of the FPI sensors were monitored during the integration of the sensor parts. When cavity length is changed constantly with piezoelectric actuators a sinusoid response as seen in Figure 6.2 is expected. Peak-to-peak amplitude of this

Table 6.1
Specifications of the manufactured FPI sensor.

Specifications	Values
Sensor Type	Extrinsic FPI
Force Type	Axial (Tip)
Measurement Range	0-13 N (max)
Resolution	<0.1 N
Size	<2 mm (Longitudinal)
MRI Compatibility	Yes

response signal is limited to 45% of the mean voltage since a beamsplitter with a splitting ratio of 55:45 is used in the optical system. Additional losses due to misalignment of the optical fibers or microdust on the reflecting surfaces significantly reduce the amplitude of the response signal. In Figure 6.2, the response of an FPI sensor without significant intensity losses was recorded as the cavity length of the sensor was increased with increments of 20 nm for a total length of 11 μm.

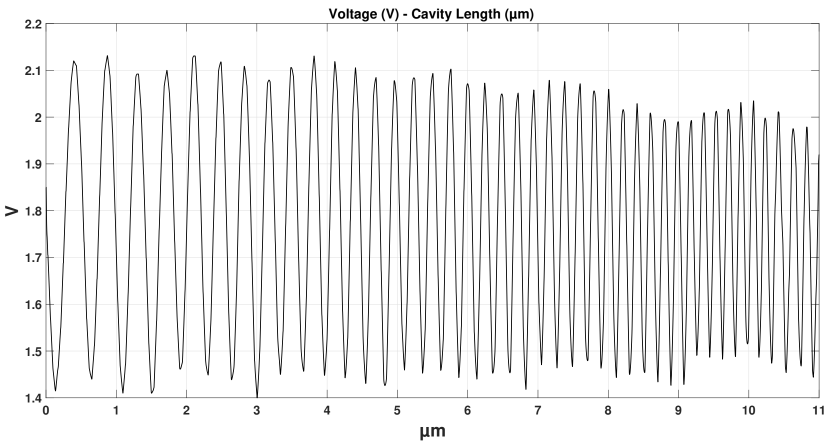

Figure 6.2 Voltage-Cavity length change.

The cumulative phase shift was calculated as given in Figure 6.3 based on the peaks in Figure 6.2. A phase linear with respect to cavity length change is expected according to the theory of FPI. However, significant losses occur in light intensity when the cavity length exceeds approximately 100 μm. Even though phase shift with respect to cavity length change given in Figure 6.3 without initial and final cavity length, it can be observed that the slope of phase shift increases initially as cavity length increases. However, it is expected that the slope of the measured phase shift becomes smaller than the slope of the calculated theoretical phase shift when cavity length increases significantly because there occurs loss of light intensity eventually.

Figure 6.3 Phase Shift with respect to cavity length change.

6.3 Force Measurement Results

After fabrication of FPI sensor was completed, it was integrated and fixed into a 18-gauge and nitinol prostate biopsy needle as illustrated in Figure 6.4.

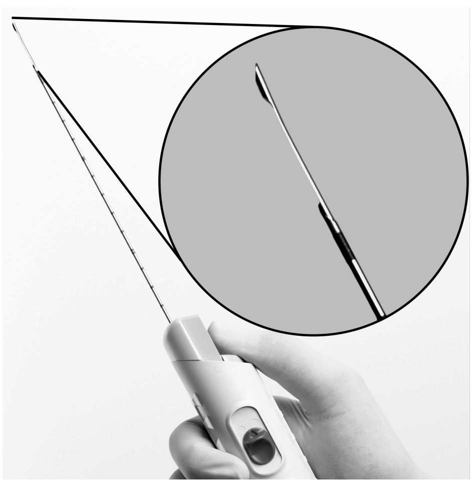

Figure 6.4 Prostate biopsy needle.

Firstly, the response of the sensors were checked with precision scales to which the sensor was placed perpendicular. Then, force measurements were taken simultaneously with force testing machine setup shown in Figure 6.5. In this measurement setup, it was critical to align the nitinol needle containing the sensor such that only axial forces were applied onto the tube and the sensor. Force range of the sensor can

Figure 6.5 Force measurement test setup.

be interpreted based on these measurements. Force measurements in Figure 6.6 shows a sensor with good peak response. The range of the sensor was approximately 7 N as the feedback signal from the sensor reaches its maximum when a force of 7 N was exerted to the sensor axially.

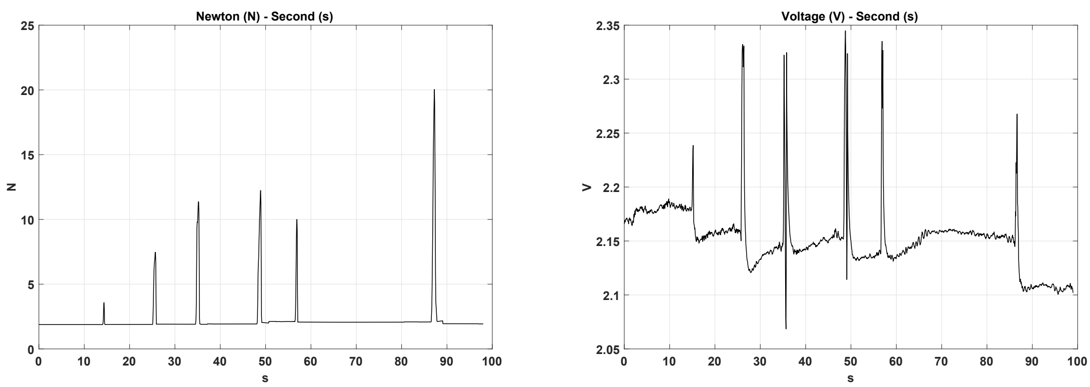

Figure 6.6 Force measurements (peak response).

When applied force exceeds the range of the sensor, phase of the signal shifts and a negative peak occurs. This might cause some signal ambiguity while interpreting the force response. The linear region of the response determines the operation range of the sensor if it is intended to operate the sensor without any signal ambiguities.

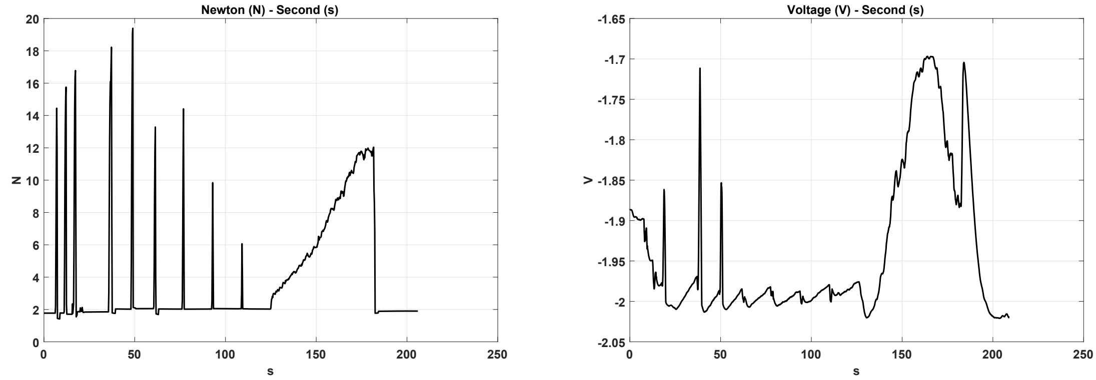

Figure 6.7 Force measurements (sensor misalignment errors).

Even though FPI sensors manufactured might be able to provide reliable output when faced with an axial force, misalignment of sensor and encapsulating nitinol needle can cause inconsistent output responses from the sensor. Some of the peak were missed by the sensor as seen in 6.7 due to errors during the test. This results also revealed that location of the sensor in biopsy needle and fixation methods should be considered for proper working of the sensor.

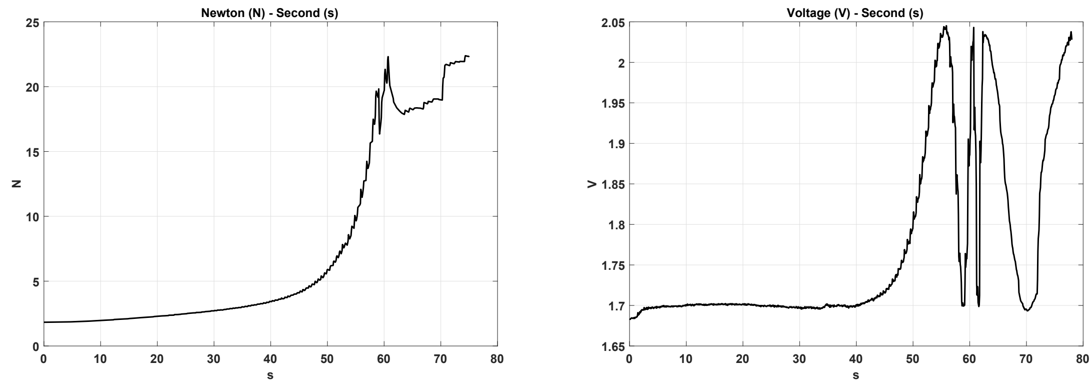

Figure 6.8 Applied force vs. sensor response.

Figure 6.8 shows another sensor performance which has a force measurement range up to 13 N. It was observed that the sensor was able to respond consistently even when this range was exceeded. If a sudden change occurs in the amount of applied force, the slope of output signal increases coherent with that force.

The output from FPI sensor given in Figure 6.9 completely matches with results from the force testing machine. The range of the sensor is limited to approximately 7 N but it provides substantially high resolution for the operation range.

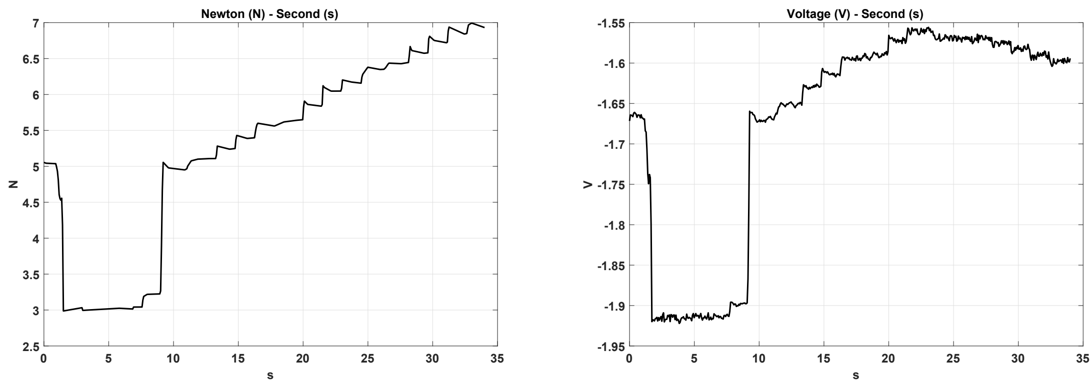

Figure 6.9 Applied force vs. sensor response.

It can be observed from Figure 6.10 that the resolution of the FPI sensor is better than 0.1 N thanks to precise detection of signal variations with photodetectors and quantization of measurements with high speed 24-bit ADCs integrated to the signal processing system. It can be concluded that a resolution that guarantees differentiation of different tissue types is achievable with the designed FPI sensor.

When the applied axial force was increased with a constant rate, the sensor reached its maximum feedback intensity. It was observed from the Figure 6.11 that the slope of the response did not change significantly as the phase of the output signal shifted with constantly increasing applied force.

Mathematical evaluation of the measurement signal in-real time can lead an FPI

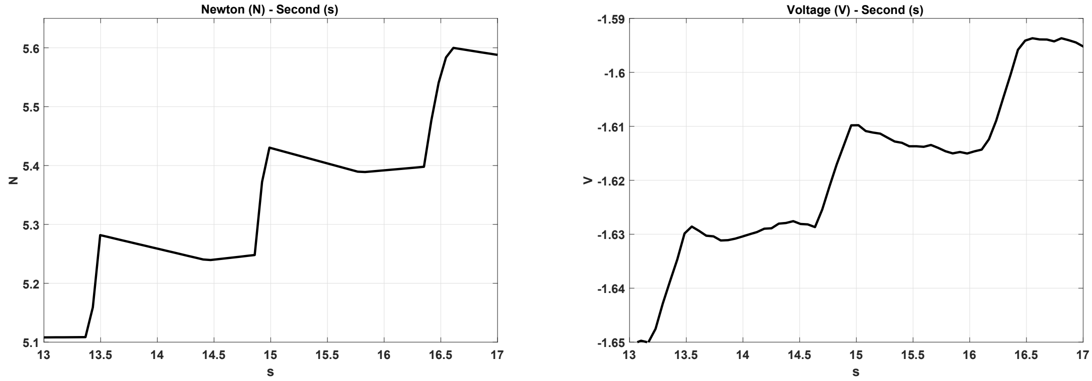

Figure 6.10 Applied force vs. sensor response.

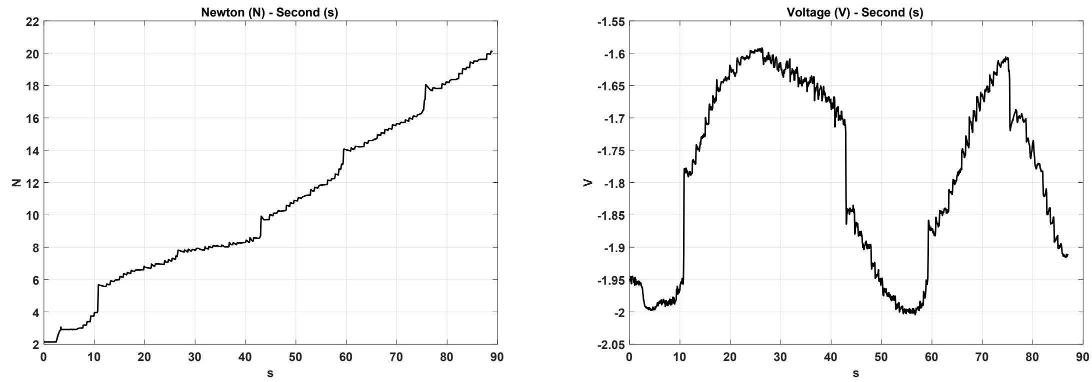

Figure 6.11 Applied force vs. sensor response.

sensor with higher ranges. Figure 6.12 and 6.13 shows force measurement by testing machine and FPI sensor respectively.

If the point where the sensor reaches its maximum measurement range in the linear range can be detected based on the phase shift observed in response signal, then the mathematical evaluation of the signal can be done accordingly. With such an approach, the sensor can be used to measure force without limiting its operation to linear region of the output signal. However, it requires an assumption that applied axial force keeps increasing at the edge of linear regions, which cannot be detected easily. Also, misinterpretations of maxima and minima of the output signal result in errors in the measurement and limits the reliability of the sensor.

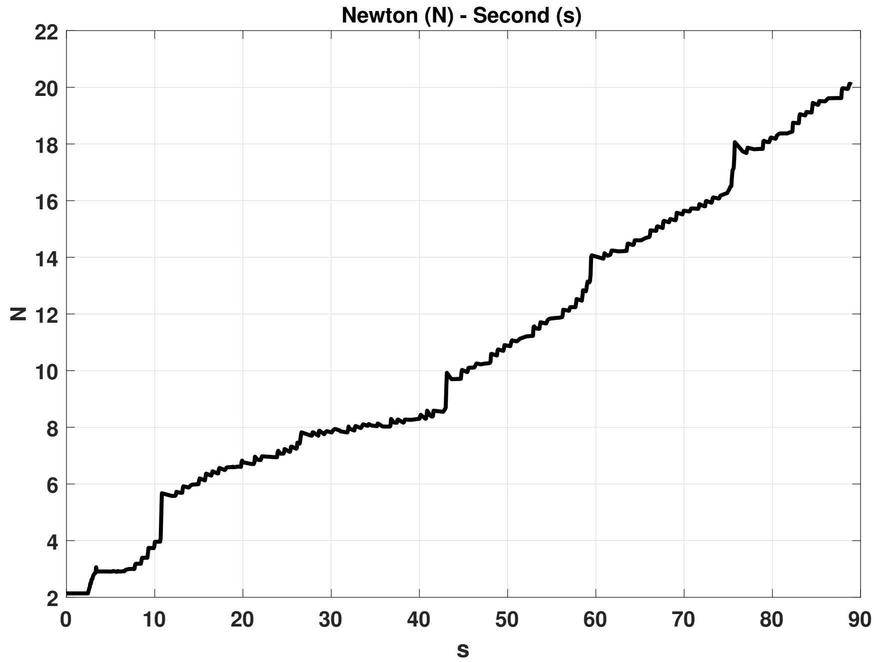

Figure 6.12 Force measurements by testing machine.

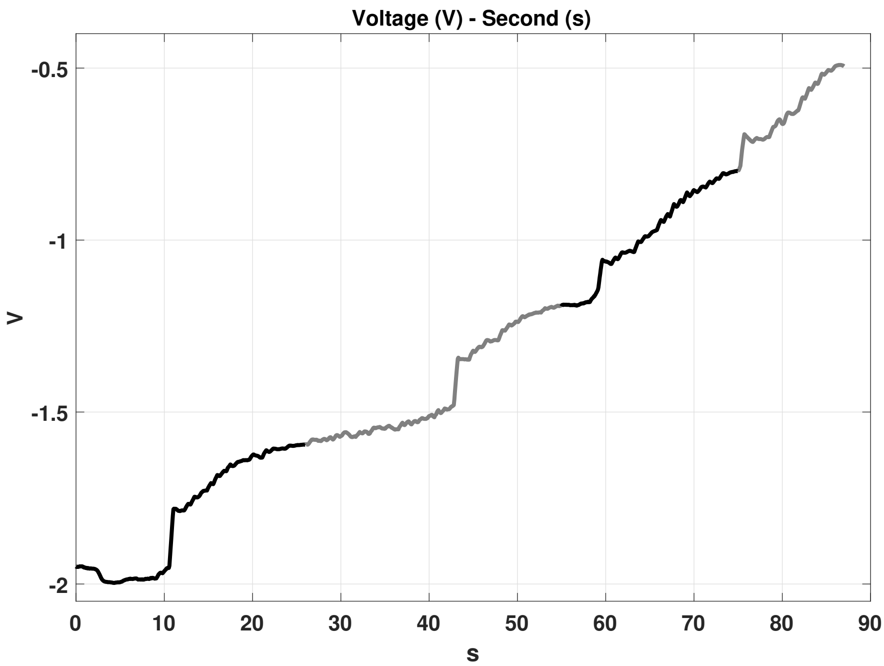

Figure 6.13 Response by FPI sensor.

7. DISCUSSION

7.1 Limitations

In general, it can be said that the manufacturing process of FPI force sensors mostly depends on manual tasks. Every sensor needs to be calibrated after manufacturing since critical parameters such as guage length, effective cavity length, and alignment angle of optical fibers varies between sensors. Temperature sensitivities of the sensors also differ from each other due to different amounts of adhesives used during manufacturing.

Angle between surface of optical fibers is one of the critical parameters which significantly affects the performance of the sensors. Fringe visibility of FPI highly depends on the angle of optical fibers that construct the FPI cavity. When it is less than 4°, fringe visibility is not affected much, and it drops to only 90% of its initial value. However, values larger than 4° cause a drastic decrease in fringe visibility, which lowers overall performance of the system in terms of measurement resolution [73]. Hence, angle between surface of optical fibers should be kept small by precise cutting, cleaving, and polishing. For the FPI sensor designed, reflective surfaces of optical fibers are formed by using a commercially available optical cleaver that is susceptible to cause some distortions on the surfaces of optical fibers. Hence, cleaving is followed by polishing of optical fibers on several layers of different friction coefficients. Finally, surface of optical fibers is visually inspected to check if it is completely diagonal to the longitudinal axis of the fiber and it has high reflectivity. However, visual inspection is not sufficient and some dust on the surface of optical fibers occurs due to lack of optimization in these procedures. Effects of misalignment of the reflective surfaces and defects on the structure might be observed during the integration of optical fibers into glass capillary.

Interference of light from a sensor with large cavity length can be approximated by two beam interferences based on the theoretical concepts explained in the previous sections. Therefore, FPI sensor becomes more ineffective to measure dynamic range changes as the cavity length increases. Even small misalignment of the optical fibers result in cascaded losses in reflected light intensity when cavity length is large. This limits the initial cavity length and that is why the dynamic range of FPI sensor is also limited. Analysis of cavity length in FPI implies that higher surface reflectivity and better collimation of light into lead-in fiber enables manufacturing FPI sensors with higher cavity length. Even though a collimating lens is integrated into the optical system for this purpose, losses in the light intensity still occurs, which limits the maximum cavity length of the sensor.

Accuracy of force sensors are strongly dependent on cross-sensitivity to temperature variations. Temperature changes cause non-linear effects on the output of mechanical and electrical force sensors while these effects are linear in optical force sensors. Temperature variations have significant effects on the effective cavity length which can be expressed as follows [71]:

$$\Delta d_F = f_1(\Delta F) + f_2(\Delta T) \tag{7.1}$$

$$\Delta d_f = \Delta d_F - k\Delta d_R \tag{7.2}$$

Δd_F represents changes in effective length due to both axial forces applied on the sensor ($f_1(\Delta F)$) and thermal expansion of the cavity materials due to temperature variations ($f_2(\Delta T)$).

8. CONCLUSION

Prostate biopsy procedure under MRI is a promising method for diagnosis of prostate cancer by means of superior soft tissue contrast of MRI and precise movement control of biopsy needle. For such procedures, force measurements at the needle tip provide real-time feedback to the operator in terms of tissue stiffness or potential needle deflection. Therefore, it increases biopsy accuracy and patient safety.

In this thesis project, a fiber optic based force measuring sensor was developed considering the MRI compliance criterion. High electromagnetic interference of MRI makes it impossible to use conventional sensors for interventional procedures under MRI to avoid image degradation, malfunction or safety issues. Using a Fabry-Pérot Interferometry (FPI) based fiber optic force sensor overcomes these problems by being immune to electromagnetic and RF interference. The FPI sensor fabricated can be classified completely MRI-compatible, meeting all of the requirements of prostate biopsy procedure under MRI.

As a light source, a laser diode which has a wavelength of 635 nm was used for the operation of the sensor. Force measurements were performed based on the interference patterns formed in the range of coherence length. It was critical to consider effects of temperature change on the operation parameters of the laser since it is a known fact current threshold conditions which is one of the main characteristics of a laser source is highly dependent on the ambient temperature. Such variations in the main characteristics of a laser result in shifts in bandwidth and wavelength of the beam emitted from the laser. The rate of motion of positive and negative charges in PN junction increases significantly increasing temperature. As a result, emission power and light intensity induced from laser falls rapidly. Therefore, the light intensity from the laser diode was kept constant during the operation by designing a fast and accurate temperature controller.

The sensor is novel in the sense that effective gauge length, which is the most crucial dimensional element determining the resolution and measurement range of the sensor, can be adjusted with high precision by changing the position of micro-holes created with laser machining. With the designed force sensor, the deviations of the bends and deviations of the needle tip from the predetermined path of travel can be detected in simultaneously and one of the most critical problems in the prostate biopsy performed under the MRI can be solved. In addition, quantitative force information measured during biopsy has potential to be used for diagnosis of prostate cancer directly.

8.1 Prospective Studies

Different concepts of improvements on the performance of the FPI sensor and optimization of manufacturing process are investigated in this section.

The sensor consists of a borosilicate glass capillary and two optical fibers which form an air cavity within the capillary. Alignment of the optical fibers inside the borosilicate glass capillary is crucial for a desirable force measurement. The reflected light from the sensing (secondary) fiber should be captured by the leading (primary) fiber with the highest efficiency possible since even the smallest angle shift between the two fibers can affect outcome drastically. In order to ensure a perfect alignment and to receive the reflected light intensity without significant losses, a multimode optical fiber with a larger diameter can be used as the sensing fiber.

Custom designed novel FPI based fiber optic force sensor provides a sufficient resolution for force measurements at the needle tip during MRI guided prostate biopsy operation. Although it is possible to ensure the accuracy and safety of the prostate biopsy operation with that initial resolution, a more advanced force sensor with a much higher resolution can be fabricated by increasing SNR of the force sensor. From the clear cleaved fiber end, only 4% of the light reflects according to the Fresnel equation [74]. Cleaved fiber ends can be Aluminum (Al) coated by sputtering for obtaining a better reflectance [75, 76]. Reflectance of the fiber ends can be increased from 4% up to 21% with Al coating. This abrupt increase in reflectance results in a much higher SNR, hence a much higher resolution for force sensing.

FPI based force sensors can be considered less sensitive to thermal effects compared to other optical force sensing technologies [74, 77, 78]. However, thermal expansion coefficients of the materials used in the structure of FPI sensor differ from each other, which results in temperature cross-sensitivity [79]. The effects of temperature on the structure of the sensor should be eliminated for reliability of measurements during prostate biopsy procedure. This can be achieved by the integration of another optical sensor onto biopsy needle to measure temperature and compensate the effects on force measurement [80, 81, 82]. Setting the temperature of the biopsy needle and FPI sensor to inner body temperature before the insertion might be a cost-effective alternative solution to compensate effects of temperature variations.

With further improvement of the Fabry-Pérot based fiber optic force sensor design, differentiation between different tissues can be achieved. Prostate cancer diagnosis by detection and differentiation of different tissue types such as tumorous and healthy tissue or malignant and benign tumorous tissue is possible using the force sensing alone, with respect to the mechanical characteristics and different tactile responses of different tissue types.

9. PUBLICATIONS

1. O. Ulgen, D. Uzun, O. Kocaturk. "Fiber Optic-Based Force Measurement Sensor Design for Prostate Biopsy Procedure under MRI," International Journal of Physical and Mathematical Sciences, ICOFS 2018: 20th International Conference on Optical Fiber Sensors, Vol:12, No:3, World Academy of Science, Engineering and Technology 2018.

APPENDIX A. PDA36A-EC Si Switchable Gain Detector

A.1 Theory of Operation

This model of photodiode was selected because it is suitable for measuring continuous wave light sources as used in the project. The sensor works based on a PIN photodiode and it includes a trans-impedance amplifier with switchable gain options.

A.2 Responsivity

The responsivity of the photodiode sensor is given in Figure A.1 and it is defined with the ratio of generated photocurrent (IPD) to the incident light power (P) at a specific wavelength as follows [83]:

$$R(\lambda) = \frac{I_{PD}}{P} \tag{A.1}$$

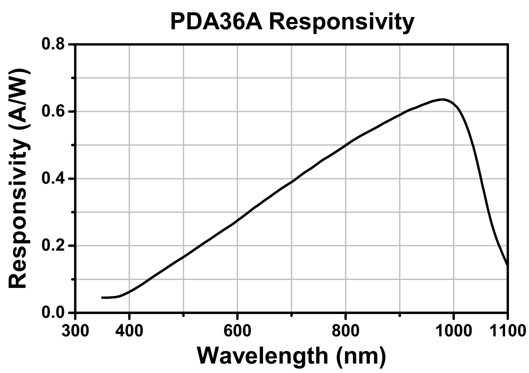

Figure A.1 Response curve.

APPENDIX B. LP635-SF8 Laser Diode

B.1 Specifications

Specifications of the laser diode used as single mode laser source for the FPI sensor is given in Figure B.1 and Figure B.2 [84]:

LD Reverse Voltage (Max)	2 V
PD Reverse Voltage (Max)	30 V
Optical Output Power	8 mW (Typ.)
Operating Temperature	0 to 50 °C
Storage Temperature	-10 to 65 °C
Pin Code	5 A
Fiber	SM600
Connector	FC/PC

Figure B.1 General specifications of LP635-SF8.

	Minimum	Typical	Maximum
Wavelength	630 nm	635 nm	645 nm
Threshold Current at 25 °C	-	45 mA	60 mA
Slope Efficiency at 25 °C	0.30 W/A	45 mA	60 mA
Operating Current @ PO = 10 mW at 25 °C	-	60 mA	80 mA
Operating Voltage @ PO = 10 mW at 25 °C	-	2.3 V	3.0 V
Monitor Current @ PO = 10 mW at 25 °C	0.10 mA	0.20 mA	0.40 mA

Figure B.2 Operating specifications of LP635-SF8.

APPENDIX C. Piezoelectric Setup

C.1 Specifications

Specifications of the piezoelectrically driven stage are given in Figure C.1 below [85]:

Travel	5 mm
Max Load	1 kg
Drive Type	Differential Micrometer & Piezo
Coarse Adjustment Pitch	0.5 mm
Fine Adjustment Range	300 μm
Fine Adjustment Pitch	50 μm
Piezo Voltage	0 to 75 V
Piezo Travel Range	20 μm range
Theoretical Resolution	20 nm (Piezo)
Feedback	N/A

Figure C.1 General specifications of NFL5DP20M.

Specifications of the piezo controller are given in Figure C.1 below:

Drive Voltage	0-150 V
Drive Current, Max, Continuous	7.5 mA
Stability	100 ppm Over 24 hrs (After 30 min Warm-Up)
Noise	<2 mV (RMS)
Typical Piezo Capacitance	1-10μF
Bandwidth	1 kHz (1 μF Load, 1 V (p-p))

Figure C.2 General specifications of KPZ101.

APPENDIX D. Fiber Port Collimator

D.1 Alignment and Coupling

The instructions for the precise and accurate collimation, alignment, and coupling of the laser beam are given below [86]:

1. The system consists of 2 fiber ports and 1 beamsplitter between them. It is necessary to carefully align the two fiber ports to collimate the light from the laser to the first fiber port and at the same time to fiber-couple through the second fiber port.
2. When the laser assembly system is connected to the fiber port, the light passing through the beam splitter travels to the second fiber port, and the 90-degree light from the beam splitter goes to the side. To align the first fiber port, first try to increase the collimation by lowering the reflected light onto a plane. For this, X-Y screws, 3 screw-line cap screws and 3 plunger screws are used on the fiber port.
3. The X and Y screws allow movement of the lens through the beam in X and Y plane. The SHC screwdriver prints at 120 degrees in the z plane and the lens can be tilted using these screws. Furthermore, when the three screws are rotated in equal amounts, the lens can be moved back and forth through z-axis. In this way, separation of the lens from the light source can be adjusted and the collimation and focal point can be precisely adjusted.

REFERENCES

1. Lau, D., Z. Chen, and J. T. Teo, "Intensity-modulated microbend fiber optic sensor for respiratory monitoring and gating during MRI," *IEEE Transactions on Biomedical Engineering*, Vol. 60(9), pp. 2655–2662, 2013.

2. Zhou, C. K., D. P. Check, J. Lortet-Tieulent, M. Laversanne, A. Jemal, J. Ferlay, and S. S.Devesa, "Prostate cancer incidence in 43 populations worldwide: an analysis of time trends overall and by age group," *International Journal of Cancer*, Vol. 138(6), pp. 1388–1400, 2016.

3. Hashim, D., P. Boffetta, C. L. Vecchia, M. Rota, P. Bertuccio, M. Malvezzi, and E. Negri, "The global decrease in cancer mortality: trends and disparities," *Annals of Oncology*, Vol. 27(5), pp. 926–933, 2016.

4. World-Health-Organization, "Estimated age-standardised rates (world) per 100,000 (2012)," 2015.

5. American-Cancer-Society, "Survival rates for prostate cancer," 2013.

6. Derweesh, I. H., P. A. Kupelian, and C. Zippe, "Continuing trends in pathological stage migration in radical prostatectomy specimens," *Urologic Oncology*, Vol. 22(4), pp. 300–306, 2004.

7. Clark, V. L., and J. A. Kruse, "Clinical methods: the history, physical, and laboratory examinations," *Journal of the American Medical Association*, Vol. 264(21), pp. 2808–2809, 1990.

8. Ghann, P. H., and M. S. C. H. Hennekens, "A prospective evaluation of plasma prostate-specific antigen for detection of prostatic cancer," *Journal of the American Medical Association*, Vol. 273(4), p. 289, 1995.

9. Tewari, A. K., and J. G. P. Whelan, *Prostate cancer: diagnosis and clinical management*, John Wiley & Sons, 2013.

10. Siddiqui, M. M., S. Rais-Bahrami, and B. Turkbey, "Comparison of MR/Ultrasound fusion-guided biopsy with Ultrasound-guided biopsy for the diagnosis of prostate cancer," *Journal of the American Medical Association*, Vol. 313(4), pp. 1390–397, 2015.

11. McCormack, M., A. Duclos, M. Latour, M. H. McCormack, D. Liberman, O. Djahangirian, and K. Zorn, "Effect of needle size on cancer detection, pain, bleeding and infection in TRUS-guided prostate biopsies: a prospective trial," *Canadian Urological Association Journal*, Vol. 6(2), p. 97, 2012.

12. Kim, C. K., "Magnetic Resonance Imaging-guided prostate biopsy: Present and future," *Korean Journal of Radiology*, Vol. 16(1), pp. 90–98, 2015.

13. Woodrum, D. A., K. R. Gorny, B. Greenwood, and L. A. Mynderse, "Men's Health: MRI-guided prostate biopsy of native and recurrent prostate cancer," in *Seminars in Interventional Radiology*, Vol. 33(3), p. 196, Thieme Medical Publishers, 2016.

14. Haffner, J., L. Lemaitre, and P. Puech, "Role of Magnetic Resonance Imaging before initial biopsy: comparison of magnetic resonance imaging-targeted and systematic biopsy for significant prostate cancer detection," *British Journal of Urology International*, Vol. 108, p. 8, 2011.

15. Ven, W. J., C. A. Hulsbergen, T. Hambrock, J. O. Barentsz, and H. J. Huisman, "Simulated required accuracy of image registration tools for targeting high-grade cancer components with prostate biopsies," *European Radiology*, Vol. 23(5), pp. 1401–1407, 2013.

16. Puech, P., O. Rouviere, R. Renard-Penna, A. Villers, P. D. P, and M. Colombel, "Prostate cancer diagnosis: Multiparametric MR-targeted biopsy with cognitive and Transrectal USMR fusion guidance versus systematic biopsy-prospective multicenter study," *Radiology*, Vol. 268, pp. 461–469, 2013.

17. Low, G., S. A. Kruse, and D. J. Lomas, "General review of Magnetic Resonance Elastography," *World Journal of Radiology*, Vol. 8(1), p. 59, 2016.

18. Chopra, R., A. Arani, Y. Huang, M. Musquera, J. Wachsmuth, M. Bronskill, and D. Plewes, "In vivo MR Elastography of the prostate gland using a transurethral actuator," *Magnetic Resonance in Medicine*, Vol. 62(3), pp. 665–671, 2009.

19. Invivo, C., "Prostate solutions," 2018.

20. Tan, N., W. C. Lin, P. Khoshnoodi, N. H. Asvadi, J. Yoshida, D. J. Margolis, and J. Huang, "In-bore 3-T MR-guided Transrectal targeted prostate biopsy: Prostate imaging reporting and data system version 2-based diagnostic performance for detection of prostate cancer," *Radiology*, Vol. 283(1), pp. 130–139, 2016.

21. Yacoub, J. H., and A. O. S. Moulton, J.S. Eggener, "Imaging-guided prostate biopsy: conventional and emerging techniques," *Radiographics*, Vol. 32(3), pp. 819–837, 2012.

22. Pokorny, M. R., M. D. Rooji, E. Duncan, F. H. Schroder, R. Parkinson, J. O. Barentsz, and L. C. Thompson, "Prospective study of diagnostic accuracy comparing prostate cancer detection by Transrectal Ultrasound-guided biopsy versus Magnetic Resonance (MR) imaging with subsequent MR-guided biopsy in men without previous prostate biopsies," *European Urology*, Vol. 66, pp. 22–29, 2014.

23. Kuru, T. H., J. J. FÃ¼tterer, J. Schiffmann, D. Porres, G. Salomon, and A. R. Rastinehad, "Transrectal Ultrasound (US), Contrast-enhanced US, real-time Elastography, Histo-Scanning, Magnetic Resonance Imaging (MRI), and MRI-US fusion biopsy in the diagnosis of prostate cancer," *European Urology Focus*, Vol. 1(2), pp. 117–126, 2015.

24. Roethke, M., A. G. Anastasiadis, M. Lichy, M. Werner, P. Wagner, S. Kruck, C. D. Claussen, A. Stenzl, H. P. Schlemmer, and D. Schilling, "MRI-guided prostate biopsy detects clinically significant cancer: analysis of a cohort of 100 patients after previous negative TRUS biopsy," *World Journal of Urology*, Vol. 30(2), pp. 213–218, 2012.

25. Tuxhorn, J. A., G. E. Ayala, and D. R. Rowley, "Reactive stroma in prostate cancer progression," *The Journal of Urology*, Vol. 166(6), pp. 2472–2483, 2001.

26. Tuxhorn, J. A., G. E. Ayala, M. J. Smith, V. C. Smith, T. D. Dang, and D. R. Rowley, "Reactive stroma in human prostate cancer: induction of myofibroblast phenotype and extracellular matrix remodeling," *Clinical Cancer Research*, Vol. 8(9), pp. 2912–2923, 2002.

27. BurnsCox, N., N. C. Avery, J. C. Gingell, and A. J. Bailey, "Changes in collagen metabolism in prostate cancer: a host response that may alter progression," *The Journal of Urology*, Vol. 166(5), pp. 1698–1701, 2001.

28. Hoyt, K., B. Castaneda, M. Zhang, P. Nigwekar, P. A. SantAgnese, J. V. Joseph, and K. J. Parker, “Tissue elasticity properties as biomarkers for prostate cancer,” *Cancer Biomarkers*, Vol. 4(5), pp. 213–225, 2008.

29. Krouskop, T. A., T. M. Wheeler, F. Kallel, B. S. Garra, and T. Hall, “Elastic moduli of breast and prostate tissues under compression,” *Ultrasonic Imaging*, Vol. 20(4), pp. 260–274, 1998.

30. Zhang, M., P. Nigwekar, B. Castaneda, K. Hoyt, J. V. Joseph, A. SantAgnese, and K. J. Parker, “Quantitative characterization of viscoelastic properties of human prostate correlated with histology,” *Ultrasound in Medicine and Biology*, Vol. 34(7), pp. 1033–1042, 2008.

31. Su, H., N. H. I. I. Iordachita, J. Tokuda, X. Liu, R. Seifabadi, and G. S. Fischer, “Fiber-optic force sensors for MRI-guided interventions and rehabilitation: A review,” *IEEE Sensors Journal*, Vol. 17(7), pp. 1952–1963, 2017.

32. Udd, E., B. William, and J. Spillman, eds., *Fiber Optic Sensors: An Introduction for Engineers and Scientists*, USA: Wiley, 2011.

33. Yasin, M., S. W. Harun, and H. Arof, *Fiber Optic Sensors*, Rijeka, Croatia: INTECH, 2012.

34. Mo, Z., W. Xu, and N. Broderick, “A Fabry-Perot optical fiber force sensor based on intensity modulation for needle tip force sensing,” in *Automation, Robotics and Applications (ICARA) 2015 6th International Conference*, Vol. 6, pp. 376–380, IEEE, 2015.

35. Yuan, L. B., L. M. Zhou, and J. S. Wu, “Fiber optic temperature sensor with duplex michelson interferometric technique,” *Sensors and Actuators*, Vol. 86, pp. 2–7, 2000.

36. Zhao, Y., and F. Ansari, “Intrinsic single-mode fiber-optic pressure sensor,” *IEEE Photonics Technology Letters*, Vol. 13, pp. 1212–1214, 2001.

37. Tian, Z., S. Yam, and H. P. Loock, “Single-mode fiber refractive index sensor based on core-offset attenuators,” *IEEE Photonics Technology Letters*, Vol. 16, pp. 1387–1389, 2008.

38. Brakel, A. V., and P. L. Swart, “Temperature-compensated optical fiber michelson refractometer,” *Optical Engineering*, Vol. 44, pp. 1576–1580, 2005.

39. Lee, B. H., Y. H. Kim, K. S. Park, J. B. Eom, M. J. Kim, B. S. Rho, and H. Y. Choi, “Interferometric fiber optic sensors,” *Sensors*, Vol. 12, pp. 2467–2486, 2012.

40. Sirkis, J. S., D. D. Brennan, M. A. Putman, T. A. Berkoff, A. D. Kersey, and E. J. Friebele, “In-line fiber etalon for strain measurement,” *Optics Letters*, Vol. 18, pp. 1973–1975, 1973.

41. Islam, R., M. M. Ali, M. Lai, K. Lim, and H. Ahmad, “Chronology of Fabry-Perot interferometer fiber-optic sensors and their applications: A review,” *Sensors*, Vol. 14(4), pp. 7451–7488, 2014.

42. Tsai, W. H., and C. J. Lin, “A novel structure for the intrinsic Fabry-Perot fiber-optic temperature sensor,” *Journal of Lightwave Technology*, Vol. 19, pp. 682–686, 2001.

43. Kim, S. H., J. J. Lee, D. C. Lee, and I. B. Kwon, “A study on the development of transmission-type extrinsic Fabry-Perot interferometric optical fiber sensor,” *Journal of Lightwave Technology*, Vol. 17, pp. 1869–1874, 1999.

44. Rao, Y., Z. Ran, and Y. Gong, *Fiber-Optic Fabry-Perot Sensors: An Introduction*, New York, USA: CRC Press, 2017.

45. Yin, S., P. B. Ruffin, and F. T. S. Yu, eds., *Fiber Optic Sensors Second Edition*, New York, USA: CRC Press, 2008.

46. Fang, Z., K. K. Chin, R. Qu, and H. Cai, *Fundamentals of Optical Fiber Sensors*, New Jersey, USA: John Wiley & Sons Inc. Publication, 2012.

47. Santos, J. L., and F. Farahi, eds., *Handbook of Optical Sensors*, USA: CRC Press, 2015.

48. Varu, H., *The optical modelling and design of Fabry-Perot Interferometer sensors for ultrasound detection.* PhD thesis, University College London, London, England, 2014.

49. Khan, H., "Fabry-Perot interferometer; construction, calibration and development," Master's thesis, University of Jyvaskyla, Jyvaskyla, Finland, 2015.

50. Bass, M., ed., *Handbook of Optics Second Edition*, California, USA: McGraw-Hill, 2001.

51. Camacho, E. F., and C. B. Alba, *Model Predictive Control Second Edition*, London, England: Springer-Verlag London, 2007.

52. Xu, J., X. Wang, K. L. Cooper, and A. Wang, "Miniature fiber optic pressure and temperature sensors," *Proceedings of SPIE - The International Society for Optical Engineering*, Vol. 6004, pp. 7–12, 2005.

53. Bremer, K., E. Lewis, G. Leen, B. Moss, S. Lochmann, I. Mueller, and J. Schrotter, "Fibre optic pressure and temperature sensor for geothermal wells," *Sensors*, Vol. 2010, pp. 538–541, 2010.

54. Zhou, X., Q. Yu, W. Peng, B. Moss, S. Lochmann, I. Mueller, and J. Schrotter, "Simultaneous measurement of down-hole pressure and distributed temperature with a single fiber," *Measurement Science and Technology*, Vol. 23(8), pp. 085–102, 2012.

55. Wang, Q., C. Qin, D. Wang, and Y. Zhao, "Investigation on stability of extrinsic Fabry-Perot interferometric pressure sensors for high-temperature/high-pressure underground applications," *Instrumentation Science and Technology*, Vol. 41(2), pp. 143–153, 2013.

56. Chen, K., X. Zhou, Y. Yang, and Q. Yu, "A hybrid Raman/EFPI/FBG sensing system for distributed temperature and key-point pressure measurements," *2015 International Conference on Optical Instruments and Technology: Optical Sensors and Applications*, Vol. 9620, p. 9620, 2015.

57. Wang, A., H. Xiao, J. Wang, Z. Wang, W. Zhao, and R. G. May, "Self-calibrated interferometric-intensity-based optical fiber sensors," *Journal of Lightwave Technology*, Vol. 19(10), p. 1445, 2001.

58. Su, H., W. Shang, G. Li, N. Patel, and G. S. Fischer, "An MRI-guided telesurgery system using a Fabry-Perot Interferometry force sensor and a pneumatic haptic device," *Annals of Biomedical Engineering*, Vol. 45(8), pp. 1917–1928, 2017.

59. Yan, K., T. Podder, L. Li, J. Joseph, D. R. Rubens, E. M. Messing, and Y. Yu, "A real-time prostate cancer detection technique using needle insertion force and patient-specific criteria during percutaneous intervention," *Medical Physics*, Vol. 36(7), pp. 3356–3362, 2009.

60. Podder, T. K., J. Sherman, D. P. Clark, E. M. Messing, D. J. Rubens, J. G. Strang, and Y. Yu, "Evaluation of robotic needle insertion in conjunction with in vivo manual insertion in the operating room," *Robot and Human Interactive Communication, 2005. ROMAN 2005. IEEE International Workshop*, Vol. 2005, pp. 66–72, 2005.

61. Podder, T. K., J. Sherman, E. M. Messing, D. J. Rubens, D. Fuller, J. G. Strang, and Y. Yu, "Needle insertion force estimation model using procedure-specific and patient-specific criteria," *Engineering in Medicine and Biology Society, 2006. EMBS'06. 28th Annual International Conference of the IEEE*, Vol. 2006, pp. 555–558, 2006.

62. Xiang, S., X. Xiang, and C. Feng, "Effects of temperature on laser diode ignition," *Optik-International Journal for Light and Electron Optics*, Vol. 120(2), pp. 85–88, 2009.

63. Ishikawa, M., H. Shiozawa, K. Itaya, G. Hatakoshi, and Y. Uematsu, "Temperature dependence of the threshold current for InGaAlP visible laser diodes," *IEEE Journal of Quantum Electronics*, Vol. 27(1), pp. 23–29, 1991.

64. Kondow, M., T. Kitatani, K. Nakahara, and T. Tanaka, "Temperature dependence of lasing wavelength in a GaInNAs laser diode," *IEEE Photonics Technology Letters*, Vol. 12(7), pp. 777–779, 2000.

65. Agrawal, G. P., and N. K. Dutta, *Semiconductor Lasers*, New York, USA: Springer Science & Business Media, 2013.

66. Prist, M., P. Cicconi, F. Ferracuti, A. C. Russo, A. Monteriu, E. Pallotta, and S. Longhi, "Temperature control of an innovative aluminium-steel molds induction preheat process placed on automated laser guided vehicles," in *Environment and Electrical Engineering and 2017 IEEE Industrial and Commercial Power Systems Europe*, pp. 1–5, IEEE, 2017.

67. Matlab, *Model Predictive Control Toolbox Getting Started Guide.*

68. Jatunitanon, P., S. Tawaytibhong, and S. W. andW. Chartlatanagulchai, "Robust model predictive controller design for thermal plate system via linear matrix inequality approach.," in *The 28th Conference of the Mechanical Engineering Network of Thailand*, Vol. 28, pp. 973–984, MENETT, 2014.

69. Huang, H., S. Fu, P. Zhang, and L. Sun, "Design of a small temperature control system based on TEC," in *Computational Intelligence and Design (ISCID), 2016 9th International Symposium*, Vol. 1, pp. 193–196, IEEE, 2016.

70. Coldren, L. A., S. W. Corzine, and M. L. Mashanovitch, *Diode lasers and photonic integrated circuits*, New Jersey, USA: John Wiley & Sons Inc. Publication, 2012.

71. Mo, Z., and W. Xu, "Temperature-compensated optical fiber force sensing at the tip of a surgical needle," *IEEE Sensors Journal*, Vol. 16(24), pp. 8936–8943, 2016.

72. Ulgen, O., D. Uzun, and O. Kocaturk, "Fiber optic-based force measurement sensor design for prostate biopsy procedure under MRI," in *International Journal of Physical and Mathematical Sciences, ICOFS 2018: 20th International Conference on Optical Fiber Sensors*, Vol. 12, p. 4, World Academy of Science, Engineering and Technology, 2018.

73. Han, M., *Theoretical and Experimental Study of Low-Finesse Extrinsic Fabry-Perot Interferometric Fiber Optic Sensors.* PhD thesis, Virginia Polytechnic Institute and State University, Blacksburg, USA, 2006.

74. Born, M., and E. Wolf, *Principles of Optics*, Pergamon Press, 1964.

75. Yoshino, T., K. Kurosawa, K. Itoh, and T. Osa, “Fiber-optic Fabry-Perot interferometer and its sensor applications,” *IEEE Journal of Quantum Electronics*, Vol. 18(10), pp. 1624–1633, 1982.

76. Hogg, W. D., D. Janzen, T. Valis, and R. M. Measures, “Development of a fiber Fabry-Perot strain gauge,” *Fiber Optic Smart Structures and Skins IV*, Vol. 1588, pp. 300–308, 1991.

77. Beekmans, S., T. Lembrechts, J. van den Dobbelsteen, and D. van Gerwen, “Fiber-optic Fabry-Perot Interferometers for axial force sensing on the tip of a needle,” *Sensors*, Vol. 17(1), p. 38, 2016.

78. Elayaperumal, S., J. H. Bae, D. Christensen, M. R. Cutkosky, B. L. Daniel, R. J. Black, and B. Moslehi, “MR-compatible biopsy needle with enhanced tip force sensing,” in *World Haptics Conference (WHC)*, Vol. 17(1), pp. 109–114, IEEE, 2013.

79. Gahler, M. C., “Forces in needle interventions: Measuring tip forces,” Master’s thesis, Technology University of Delft, Delft, Netherlands, 2012.

80. Yu, Q., and X. Zhou, “Pressure sensor based on the fiber-optic extrinsic Fabry-Perot interferometer,” *Photonic Sensors*, Vol. 1(1), pp. 72–83, 2011.

81. Mo, Z., and W. Xu, “Temperature-compensated optical fiber force sensing at the tip of a surgical needle,” *IEEE Sensors*, Vol. 16(24), pp. 8936–8943, 2016.

82. Zhou, A., B. Qin, Z. Zhu, Y. Zhang, Z. Liu, J. Yang, and L. Yuan, “Hybrid structured fiber-optic Fabry-Perot interferometer for simultaneous measurement of strain and temperature,” *Optics Letters*, Vol. 39(18), pp. 5267–5270, 2014.

83. Thorlabs, *PDA36A(-EC) Si Switchable Gain Detector User Guide.*

84. Thorlabs, *LP635-SF8, Pigtailed Laser Diode, SMF.*

85. Thorlabs, *NFL5 Series 5.0 mm Travel Single Axis Flexure Stages.*

86. Thorlabs, *PAF Series Aspheric and Achromatic FiberPort Collimators with FC/PC, FC/APC, or SMA Adapters User Guide.*